

# **Diploma Thesis**

## Development of a Purity Monitor with a Beta Source and Study of a Spontaneous Fission Source

Paolo Crivelli, Institute for Particle Physics, ETHZ, Switzerland

Under supervision of:  
Prof. Dr. André Rubbia  
Dr. Andreas Badertscher

October 10, 2001

## **Abstract**

In this report the development of a purity monitor employing a positron source ( $^{22}\text{Na}$ ) and the measurements are described. The applicability of a spontaneous fission source ( $^{252}\text{Cf}$ ) to a new type of purity monitor is studied. The basic principle for both purity monitors is the same: the particles emitted ionize the liquid Argon, producing free electrons which are drifted in an electric field with a suitable geometry, dependent on the source. Measuring the initial charge, the drift time and the charge collected at the anode one can calculate the mean life time of the electrons in liquid LAr.

# Contents

<b>1</b>	<b>Introduction</b>	<b>3</b>
1.1	The Icarus project . . . . .	3
1.2	Importance of the purity monitor . . . . .	5
1.3	The Purity Monitor Design . . . . .	5
<b>2</b>	<b>Theory</b>	<b>8</b>
2.1	Design of a Beta source . . . . .	8
2.1.1	Theory of beta decay . . . . .	8
2.1.2	Stopping power and range of positrons in LAr . . . . .	10
2.1.3	The $^{22}\text{Na}$ -cell . . . . .	16
2.2	Considerations about a spontaneous fission source: $^{252}\text{Cf}$ . . . . .	18
2.2.1	Theory of the fission . . . . .	18
2.2.2	The electronic stopping power of high velocity heavy ions . . . . .	21
2.2.3	The SRIM simulation . . . . .	24
<b>3</b>	<b>Calculation of the number of free electrons and choice of the field configuration</b>	<b>27</b>
3.1	The recombination effect . . . . .	27
3.2	The Beta source . . . . .	28
3.2.1	Expected number of free electrons . . . . .	28
3.2.2	The electric field . . . . .	29
3.3	The spontaneous fission source . . . . .	31
3.3.1	Expected number of free electrons . . . . .	31
3.3.2	The electric field . . . . .	31
<b>4</b>	<b>Monte Carlo simulation of the drift time and the signal width</b>	<b>33</b>
4.1	The drift velocity . . . . .	33

4.1.1	The diffusion . . . . .	34
4.2	Results . . . . .	35
4.2.1	The $^{22}\text{Na}$ -cell . . . . .	35
4.2.2	The $^{252}\text{Cf}$ -cell . . . . .	36
<b>5</b>	<b>Experimental Set-up</b>	<b>39</b>
5.1	Mechanics of the purity monitor . . . . .	39
5.1.1	The $^{22}\text{Na}$ -cell . . . . .	39
5.1.2	Deposition of the source on the cathode . . . . .	43
5.2	The LAr filling procedure . . . . .	44
5.3	Electronics . . . . .	46
5.3.1	The preamplifier . . . . .	46
5.3.2	The active band pass filters . . . . .	46
5.3.3	The offset and the $\pm 1\text{V}$ adaptor . . . . .	48
5.3.4	Test channel . . . . .	50
<b>6</b>	<b>Measurements</b>	<b>51</b>
6.1	Data Acquisition and Analysis . . . . .	51
6.2	Measurements . . . . .	52
6.2.1	Trigger at the cathode . . . . .	53
6.2.2	Trigger on the anode . . . . .	57
6.3	Discussion of the measured charge distribution . . . . .	58
<b>7</b>	<b>Conclusions</b>	<b>64</b>

# Chapter 1

## Introduction

### 1.1 The Icarus project

The ICARUS (Imaging Cosmic And Rare Underground Signal) experiment [7] will take place at the Gran Sasso National Laboratory near Rome, Italy. A novel liquid argon drift chamber was developed as a particle detector. The ICARUS program addresses many fundamental issues:

- the nature of neutrinos, in particular the question of the neutrino mass. This is being investigated in ICARUS both through the study of atmospheric neutrinos and through long baseline studies with the foreseen CERN neutrino beam;
- the stability of the nucleon, which is the only way to access phenomena at the energy scale of Grand Unification. ICARUS will be the first high-resolution imaging study of such a phenomenon;
- the study of solar neutrinos. Even though ICARUS is not optimized to study this kind of events, the issue remains extremely interesting and with a suitable neutron shielding ICARUS can reach a reasonable detection threshold;
- the detection of astrophysical and cosmological neutrinos from supernovae.

As a LAr TPC (time projection chamber), ICARUS has the advantage of being operated over a very large sensitive volume, continuously sensitive,

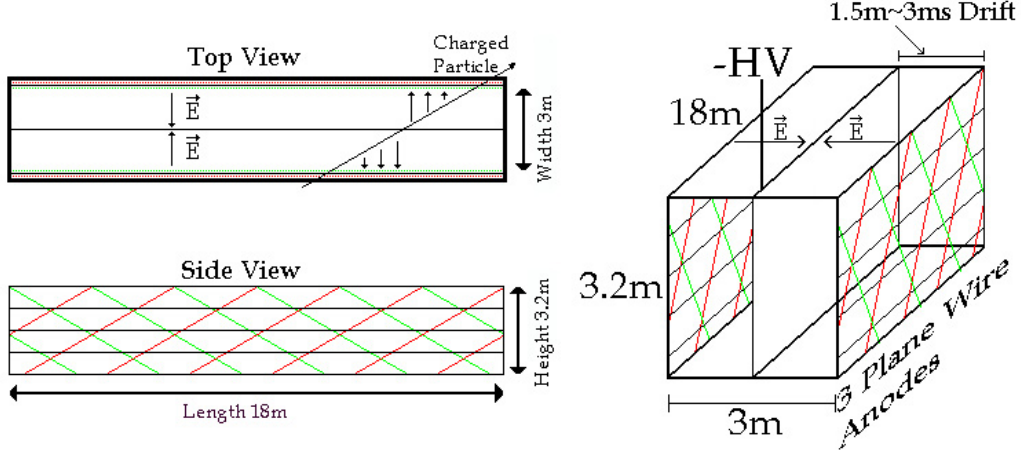


Figure 1.1: Schematic view of a 300t halfmodule of the ICARUS experiment. The drift field is  $E=500\text{V/cm}$  yielding a drift velocity  $v_{\text{drift}} = 0.5\text{mm}/\mu\text{s}$ .

self-triggering, able to provide three-dimensional views of ionizing events with particle identification from  $dE/dx$  and range measurements. At the same time, the detector acts also as a homogeneous calorimeter of very fine granularity and high accuracy. The ICARUS project requires a sensitive LAr mass of the order of several kilotons, therefore, this type of detector can be considered as an ideal device for a rare event search.

A modular approach was adopted to reach this sensitive mass, with modules as big as possible, but still able to be moved from the construction site to the Gran Sasso Laboratory. Each module of 600t LAr is composed of two sub-modules of 300t each (see picture 1.1), which can be transported by truck.

The first 600t module has been assembled at Pavia and one of the 300t halfmodules was successfully tested. It is planned to be moved to the Gran Sasso Laboratory next year. It allows an important first step in the ICARUS scientific program [1]. In fact, this detector has enough mass to investigate the atmospheric and solar neutrinos; while a much larger sensitive mass of thousands of tons is needed to detect astrophysical neutrinos, to achieve the  $10^{34}$  years range in proton decay life time and to detect the (oscillating-)neutrinos coming from the long baseline neutrino beam at CERN.

The operating principle of the ICARUS liquid argon TPC is rather simple: any ionizing event (from particle interaction or decay), taking place in

a volume of liquid argon, produces ion-electron pairs. A fraction of them will not recombine and will drift parallel to the uniform E-field (applied in opposite directions, see picture 1.1). Only the motion of the much faster electrons induces a measurable current on a number of parallel wire planes located at the end of the sensitive volume. The orientation of the wires of the three planes with respect to the horizontal direction is  $+60^\circ$ ,  $0^\circ$  and  $-60^\circ$  and together with a measurement of the drift time, provide a full 3-D image reconstruction of the event.

The LAr, used as absorber and active detector, was chosen by the following considerations:

1. it is an excellent electric insulator and available at an extremely high purity level;
2. the ionization density is high enough to get measurable pulse heights even for minimum ionizing particles.
3. it is easily available in large quantities because of its high abundance (about 1%) as a natural component of the Earth's atmosphere; it is thus cheaper than other heavy noble gases.

## 1.2 Importance of the purity monitor

The purity of the LAr is fundamental in order to reach long drift paths in the TPC. Electronegative impurities capture the electrons, and hence, decrease the charge measured with the wire chambers at the end of the drift. The purity of LAr decreases in time due to outgassing of the dewar walls and detector materials, thus, the LAr has to be circulated through a purification stage and the mean life time of the drifting electrons has to be monitored continuously, in order to keep the purity at the level necessary for a good operation of the TPC. From the parameters of the 300t module follows that life times of the order of ms are needed.

## 1.3 The Purity Monitor Design

The basic concept of the two purity monitors is the same. The particles emitted from a radioactive element ionize the liquid Argon producing free

electrons, which are then drifted in an electric field with a suitable geometry, dependent on the source type. Measuring the initial charge, the drift time and the charge collected at the anode, one can calculate the life time of the electrons. Assuming the impurities to be homogeneously distributed in the liquid, the electron capture rate is constant along the drift path. Consequently, the number of free electrons decreases exponentially with a mean life time  $\tau$ , which is dependent on the LAr purity. Thus, one can write:

$$Q = Q_0 \cdot e^{-\frac{t_{drift}}{\tau}} \quad (1.1)$$

where  $Q_0$  is the initial charge,  
 $Q$  is the remaining charge after a drift time  $t_{drift}$ ,  
 $\tau$  is mean life time of  $e^-$  in LAr.

With eq.(1.1) the mean life time  $\tau$  can easily be found:

$$\tau = -\frac{t_{drift}}{\ln \frac{Q}{Q_0}} \quad (1.2)$$

The two cells differ in their geometry which depends on the range of the emitted particles.

For the  $^{252}\text{Cf}$  source the electric field is generated by two spheres [4]. This geometry has the advantage of reducing the high recombination rate of electron-ion pairs because the E-field near the surface of the sphere is huge. The fission fragments have energies of 60–110 MeV [5] and range in LAr in the order of 18–29  $\mu\text{m}$  (simulated with SRIM programm [3], see table 3.2) and consequently their ionization density is enormous compared to  $\alpha$  or  $\beta$  particles. Another advantage of such an inhomogeneous field is that the drift time is larger than for a planar capacitor [6] with the same distance of the electrodes, because in the central region the field is very low (see section 3.2.2). A long drift region is needed to measure with a good precision the life time  $\tau$ .

The idea of employing a beta source is not new [6], contrary to that of using a spontaneous fission fragment, but in the earlier purity monitors with a beta source (see Fig.1.2 [6]) the electric field was constant. In the  $^{22}\text{Na}$ -cell the anode is a sphere of 3 mm diameter and the cathode is a disk of 93 mm diameter so that the electric field takes the form sketched in Fig.3.1, increasing the electrons drift time compared to the  $^{207}\text{Bi}$ -cell of [6].

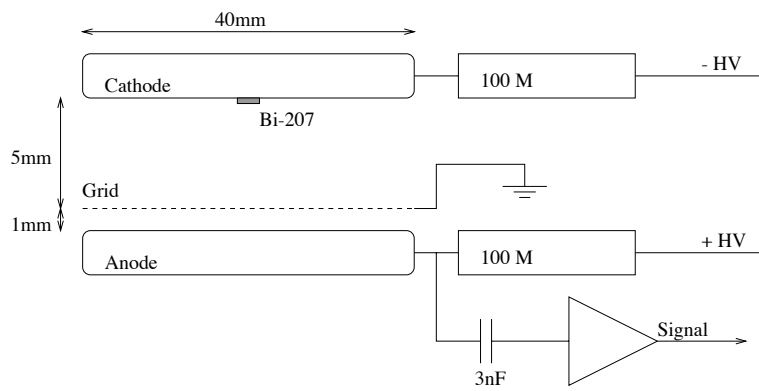


Figure 1.2: Purity monitor for the ATLAS experiment using a  $^{207}\text{Bi}$  source

# Chapter 2

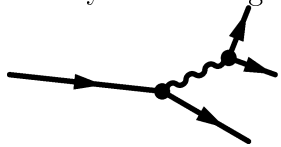
## Theory

### 2.1 Design of a Beta source

The advantage of employing a beta source is that the emitted positrons have a lower ionization density compared to an  $\alpha$ -particle or to an ion (see section 2.2) so that the recombination effect is much smaller (see section 3.1). This allows to apply a lower voltage to the electrodes, thus, the drift time can be increased.

#### 2.1.1 Theory of beta decay

The beta decay of a neutron  $n \rightarrow p + e^- + \bar{\nu}_e$  or a proton  $p \rightarrow n + e^+ + \nu_e$  in a nucleus is mediated by the weak interaction gauge bosons  $W^\pm$ , as sketched in the Feynmann diagram.



If we assume that the neutron and the proton are point like particles we can calculate the decay rate for electrons and positrons from Fermi's Golden Rule (see for example [9] at page 92):

$$d\Gamma = \frac{1}{2E} \overline{|\mathcal{M}|^2} dQ \quad (2.1)$$

With the invariant phase space  $dQ$ :

$$dQ = \frac{d^3 p_n}{(2\pi)^3 2E_n} \frac{dp_e^3}{(2\pi)^3 2E_e} \frac{dp_\nu^3}{(2\pi)^3 2E_\nu} (2\pi)^4 \delta^4(p_n - p_e - p_\nu) \quad (2.2)$$

or, integrating over  $d^3 p_n$  using  $\int d^3 p_n / 2E_n = \int d^4 p_n \theta(E_n) \delta(p_n^2)$

$$dQ = \frac{dp_e^3}{(2\pi)^3 2E_e} \frac{dp_\nu^3}{(2\pi)^3 2E_\nu} d^3 p_\nu (2\pi) \delta(E_o - E_e - E_\nu) \quad (2.3)$$

and the invariant amplitude averaged over the spin directions:

$$\overline{|\mathcal{M}|^2} = G^2 \sum_{spins} |\bar{u}(p_\nu) \gamma^0 (1 - \gamma^5) v(p_e)|^2 \quad (2.4)$$

where  $E_o$  is the kinetic energy released to the lepton pair,  
 $G \simeq 10^{-5}/m_N^2$  is the Fermi coupling constant,  
 $m_N$  the nucleon mass,  
 $\bar{u}(p_\nu)$  and  $v(p_e)$  are the Dirac spinors of the positron and of the neutrino,  
 $\gamma^0$  and  $\gamma^5$  are Dirac matrices.

The summation over spins can be performed neglecting the electron mass and using the trace theorems:

$$\sum_{spins} |\bar{u}(p_\nu) \gamma^0 (1 - \gamma^5) v(p_e)|^2 = 8E_e E_\nu (1 + v_e \cos \theta) \quad (2.5)$$

where  $\theta$  is the angle between the two leptons and  $v_e \simeq 1$  for a relativistic electron. Substituting the equations (2.3), (2.4) and (2.5) in (2.1), replacing  $d^3 p_\nu d^3 p_e$  by  $(2\pi d \cos \theta p_e^2 dp_e)(4\pi E_\nu^2 dE_\nu)$  and integrating over the four momentum of the neutrino and over  $\theta$ , one obtains the positron spectrum:

$$\frac{d\Gamma}{dp_e} = \frac{G^2}{\pi^3} p_e^2 (E_o - E_e)^2 \quad (2.6)$$

where  $E_o$  is the nuclear energy difference which determines the end point energy of the emitted particle (see Tab.2.1 for different elements). The spectrum of the beta particle is continuous and has been calculated for the positrons of  $^{22}\text{Na}$  and plotted in Figs. 2.3 and 2.4.

Table 2.1: End point and half life for various elements that emit beta particles

Element	Decay mode	Half life	End point energy (Mev)	Intensity (%)
<sup>14</sup> C	$\beta^-$	5730y	0.157	100
<sup>22</sup> Na	$\beta^+$	2.6y	0.546	90.5
			1.820	0.06
	ec		9.5	
<sup>36</sup> Cl	$\beta^-$	3.0210 <sup>5</sup> y	0.710	98.1
	ec		1.9	
<sup>42</sup> K	$\beta^-$	12.4 h	1.684	0.35
			1.997	18.4
			3.521	81.1
<sup>60</sup> Co	$\beta^-$	5.27y	0.318	99.9
			1.491	0.1
<sup>137</sup> Cs	$\beta^-$	30y	0.512	94.6
			1.173	5.4
<sup>207</sup> Bi	ec	31.8y	0.481	2
			0.975	7
			1.047	2
	$\gamma$			78

### 2.1.2 Stopping power and range of positrons in LAr

The stopping power is the average rate at which charged particles lose energy at any point along their tracks.

The total stopping power splits into two components: the collision stopping power and the radiative stopping power.

The collision stopping power is due to the energy transfer from the incident particle to bound atomic electrons. With the Bethe theory, which considers a particle interacting with a quantum harmonic oscillator and solves it in first Born approximation, it can be expressed as:

$$\frac{1}{\rho}S_{col} = NZ \int W \frac{d\sigma}{dW} \quad (2.7)$$

where  $\rho$  is the density of the medium,  
 $\frac{d\sigma}{dW}$  is the differential cross section for collisions,  
 $N$  is the number of atoms per gram of the medium,  
 $W$  is the energy transfer to atomic electrons per inelastic collision,  
 $Z$  is the atomic number of the medium.

$W$  is divided into two ranges, depending on whether it is smaller or larger than a cutoff value  $W_c$ , which has to be larger than the binding energy of the atomic electrons. For energy losses smaller than  $W_c$  the impact parameter must be large compared to atomic dimensions.

The collision stopping power is then a sum of two components:

$$\frac{1}{\rho}S_{col} = \frac{1}{\rho}S_{col}(W < W_c) + \frac{1}{\rho}S_{col}(W > W_c) \quad (2.8)$$

The main result of the Bethe theory, applicable to electrons, positrons and heavy charged particles, is the following:

$$\frac{1}{\rho}S_{col}(W < W_c) = 0.153536 MeVcm^2 g^{-1} \frac{1}{\beta^2} \frac{Z}{A} z^2 \left[ \ln\left(\frac{2mc^2\beta^2 W_c}{(1-\beta^2)I}\right) - \beta^2 \right] \quad (2.9)$$

where  $I$  is the mean excitation energy of the medium and  $z$  is the projectile charge.

Equation (2.9) is valid only when the velocity of the incident particle is large compared to the velocity of the atomic electrons.

Close collisions contribute to the stopping power with a component that can be evaluated assuming the atomic electrons to be free and at rest:

$$\frac{1}{\rho}S_{col}(W > W_c) = NZ \int_{W_c}^{W_m} W \frac{d\sigma}{dW} \quad (2.10)$$

where  $W$  is the energy transfer in a collision with a free electron and

$$W_m = 2\tau(\tau + 2)mc^2 / [1 + 2(\tau + 1)(m/M) + (m/M)^2] \quad (2.11)$$

is the largest possible energy transfer. In this equation  $\tau$  is the ratio of the projectile kinetic energy  $T$  and its rest energy and  $m/M$  is the ratio of

the electron and the projectile masses.

For positrons the energy transfer in the collision is governed by the Bhabha cross section which takes into account relativity and spin effects and is given by (see [10]):

$$d\sigma = \frac{2\pi e^4}{m\beta^2 c^2} \frac{dW}{W^2} \left[ 1 - \frac{\gamma^2 - 1}{\gamma^2} \frac{W}{T} + \frac{1}{2} \left( \frac{\gamma - 1}{\gamma} \right)^2 \left( \frac{dW}{W} \right)^2 \right. \\ \left. - \left( \frac{\gamma - 1}{\gamma + 1} \right) \left( \frac{W}{T} \right) \left\{ \frac{\gamma + 2}{\gamma} - 2 \frac{\gamma^2 - 1}{\gamma^2} \left( \frac{W}{T} \right) + \left( \frac{\gamma - 1}{\gamma} \right)^2 \left( \frac{W}{T} \right)^2 \right\} \right. \\ \left. + \left( \frac{\gamma - 1}{\gamma + 1} \right)^2 \left( \frac{W}{T} \right)^2 + \left\{ \frac{1}{2} + \frac{1}{\gamma} + \frac{3}{2\gamma^2} - \left( \frac{\gamma - 1}{\gamma} \right)^2 \left( \frac{W}{T} \right) \left( 1 - \frac{W}{T} \right) \right\} \right] \quad (2.12)$$

With the Bhabha cross section and using Eqs. (2.7), (2.8), (2.11) and correcting the formula for the density effect (which accounts for the reduction of the stopping power due to the polarisation of the medium caused by the passage of a charged particle) and improving the first Born approximation, one obtains :

$$\frac{1}{\rho} S_{col} = 0.153536 MeV cm^2 g^{-1} \frac{1}{\beta^2} \frac{Z}{A} \left[ \ln \left( \frac{T}{I} \right)^2 - \ln \left( 1 + \frac{\tau}{2} + F(\tau) - \delta \right) \right] \quad (2.13)$$

where  $F(\tau) = 2 \ln 2 - (\beta^2/12)[23 + 14/(\tau + 2) + (\tau + 2)^2 + 4/(\tau + 2)^3]$  and  $\delta$  is the density effect correction.

The radiative stopping power can be expressed in terms of the cross section for bremsstrahlung as:

$$\frac{1}{\rho} S_{rad}(T) = \frac{1}{uA} \left[ \int_0^T k \frac{d\sigma_n}{dk} dk + Z \int_0^{T'} k \frac{d\sigma_e}{dk} dk \right] \quad (2.14)$$

where  $d\sigma_n/dk$  is the differential cross section for the emission of a photon due to the interaction of the electron with the screened Coulomb field of the nucleus and  $d\sigma_e/dk$  is the cross section due to the Coulomb interaction with one of the atomic electrons.  $T'$  is the maximum energy of the emitted photon in an electron–electron interaction and is given by:

$$T' = mc^2 T [T + 2mc^2 - \beta(T + mc^2)]^{-1} \quad (2.15)$$

The difference between electron and positron stopping powers is caused by the fact that the latter is repelled by the nuclear charge and attracted by the atomic electrons; this difference is important only at low energies ( $< 0.1 \text{ MeV}$ ).

As shown in Fig.2.1, the total stopping power is maximal for the lowest positron energy and has a minimum at 1 MeV. The radiative stopping power is negligible at low energies (see Tab.2.2), but it becomes dominant for highly relativistic positrons ( $E > 50 \text{ MeV}$ ).

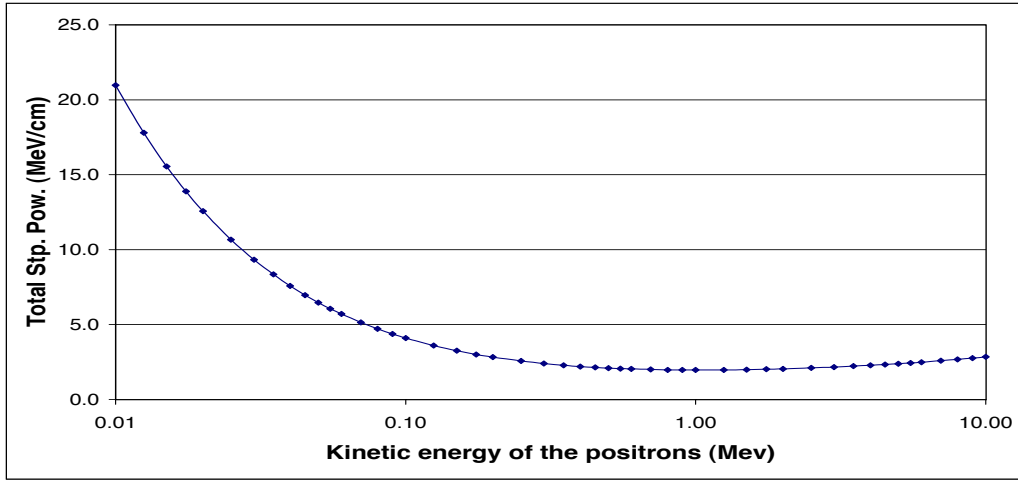


Figure 2.1: Stopping power of the positrons in LAr as a function of their kinetic energy [2]

The ranges can be obtained in the slowing down approximation (CSDA). In this approximation the energy loss fluctuation is neglected and the electrons are assumed to lose their energy continuously along the track, with a mean energy loss per unit length given by the stopping power. The range in  $g \cdot \text{cm}^{-2}$  is evaluated with:

$$r_o(T_o \rightarrow T_f) = \rho \int_{T_f}^{T_o} [S_{col}(T) + S_{rad}(T)]^{-1} dT \quad (2.16)$$

where  $T_i$  and  $T_f$  are the initial and the final energy which is set equal to the lowest atomic ionization potential if one wants to calculate how far the electron can travel.

In the ICRU REPORT 37 [2] the evaluation of the collision, the radiation stopping power and the ranges calculated with the Eqs.(2.13), (2.14), (2.16) are listed in tables for many elements. The values for positrons in Argon are reported in Tab.2.2. Note, that the density effect for energies  $< 3MeV$  is negligible ( $\delta$  is equal 0 in (2.13)) . The mean ionization potential used is  $I = 1.88MeV$  and the ranges have been corrected multipling those taken from [2] with the density of the liquid Argon  $\rho = 1.4g/cm^3$  (see last two colums of table 2.2).

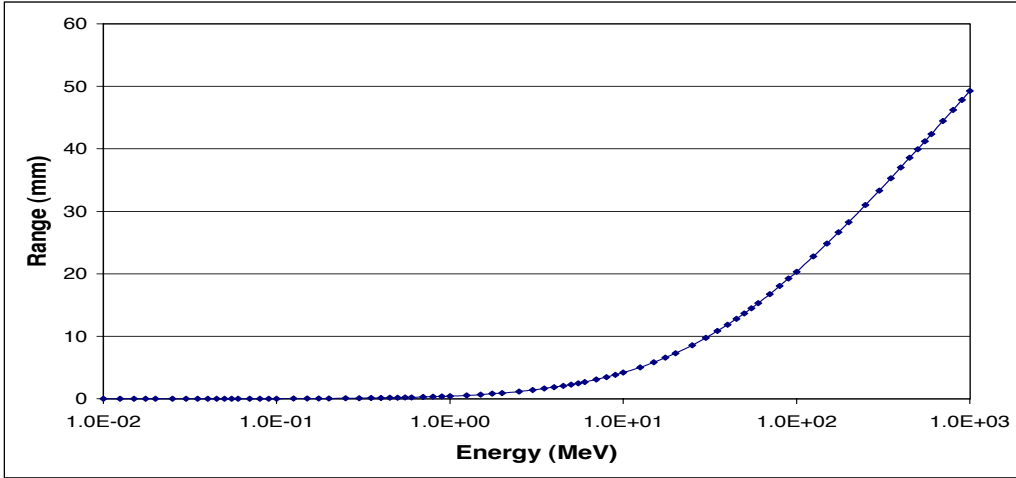


Figure 2.2: Range of positrons in LAr as a function of their kinetic energy [2]

Table 2.2: Stopping powers and ranges for positrons in Argon

Kinetic Energy MeV	Collision Stp. Pow. MeV cm <sup>2</sup> /g	Radiative Stp. Pow. MeV cm <sup>2</sup> /g	Total Stp. Pow. MeV cm <sup>2</sup> /g	CSDA Range g/cm <sup>2</sup>	Range in LAr mm
$1 \cdot 10^{-2}$	14.9	$8.1 \cdot 10^{-3}$	14.9	$3.9 \cdot 10^{-4}$	$2.8 \cdot 10^{-3}$
$5 \cdot 10^{-2}$	4.6	$9.5 \cdot 10^{-3}$	4.6	$6.2 \cdot 10^{-3}$	$4.4 \cdot 10^{-3}$
0.1	2.9	$1.0 \cdot 10^{-2}$	2.9	$2 \cdot 10^{-2}$	0.1
0.2	2.0	$1.1 \cdot 10^{-2}$	2.0	$6.3 \cdot 10^{-2}$	0.4
0.3	1.7	$1.2 \cdot 10^{-2}$	1.7	0.12	0.8
0.4	1.5	$1.4 \cdot 10^{-2}$	1.5	0.18	1.3
0.5	1.5	$1.6 \cdot 10^{-2}$	1.5	0.24	1.7
0.6	1.4	$1.8 \cdot 10^{-2}$	1.4	0.31	2.2
0.7	1.4	$2.0 \cdot 10^{-2}$	1.4	0.38	2.7
0.8	1.4	$2.2 \cdot 10^{-2}$	1.4	0.45	3.2
0.9	1.4	$2.5 \cdot 10^{-2}$	1.4	0.52	3.7
1	1.4	$2.7 \cdot 10^{-2}$	1.4	0.59	4.2
1.25	1.4	$3.4 \cdot 10^{-2}$	1.4	0.77	5.5
1.5	1.4	$4.1 \cdot 10^{-2}$	1.4	0.94	6.7
1.75	1.4	$4.8 \cdot 10^{-2}$	1.4	1.1	7.8
2	1.4	$5.6 \cdot 10^{-2}$	1.4	1.3	9.2
10	1.7	0.36	2.0	5.8	41.4
100	2.1	4.6	6.7	28.5	203.5
1000	2.4	50.1	52.4	68.9	492.1

### 2.1.3 The $^{22}\text{Na}$ -cell

For our monitor the radioactive source has been chosen by the following criteria:

- sufficiently long half life time (of the order of years);
- energies of the emitted particle as high as possible;
- available from our supplier (Isotrack);
- easy to deposit on a spherical holder;

The  $^{22}\text{Na}$  has been considered the best candidate (Tab.2.1), it has a half life time of 2.6 years and its decay modes are illustrated in 2.5. The positron energy distribution for both decays have been calculated with (2.6) using the end point energies  $E_o = 1.83$  MeV and 0.543 MeV, dependent on the decay mode. The spectra are shown in Figs. 2.3 and 2.4. According to the Fig.2.5, there occurs also electron capture, followed by a 1.274 MeV  $\gamma$  emission with a probability of 9.4%.

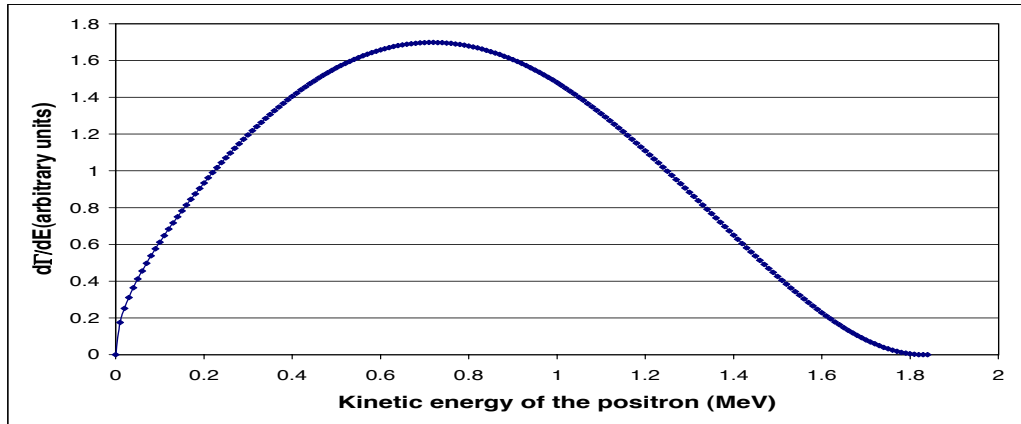


Figure 2.3: Spectrum of the positron emitted by  $^{22}\text{Na}$  with an end point kinetic energy of 1.83MeV

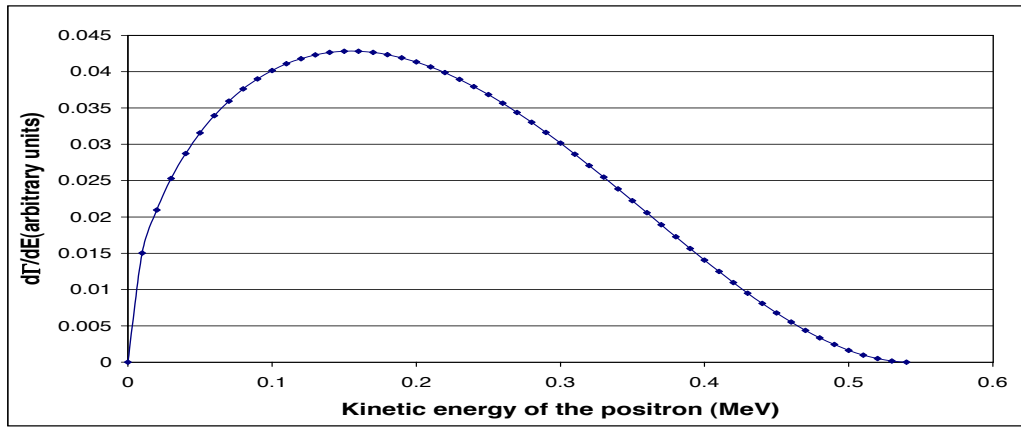


Figure 2.4: Spectrum of the positron emitted by  $^{22}\text{Na}$  with end point energy of 0.5MeV

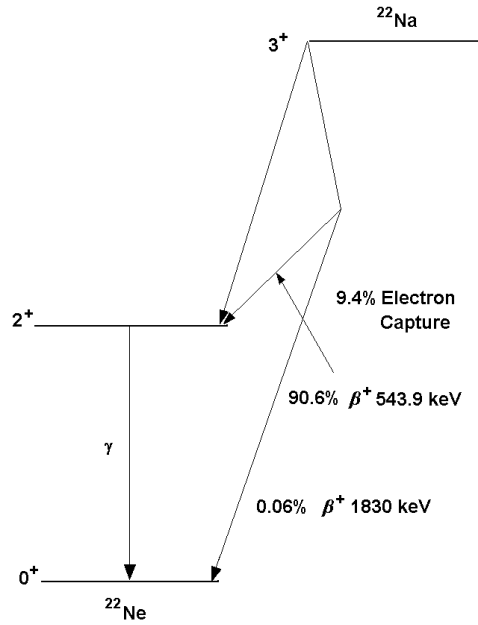


Figure 2.5: Decay scheme of  $^{22}\text{Na}$

## 2.2 Considerations about a spontaneous fission source: $^{252}\text{Cf}$

### 2.2.1 Theory of the fission

For a nucleus in its ground state it is possible to quantum mechanically tunnel through the fission barrier. This barrier can be understood as a first approximation with the liquid drop model which predicts the mass equation:

$$\Delta M = a_V \cdot A - a_A \cdot \frac{(A - 2Z)^2}{A} + a_P \frac{1}{A^{\frac{1}{2}}} - a_F \cdot A^{\frac{2}{3}} - a_C \frac{Z(Z - 1)}{A^{\frac{1}{3}}} \quad (2.17)$$

The first term proportional to the volume expresses the fact that the nuclear binding energy is proportional to the number of nucleons. This term is independent of a distortion of the shape of the nucleus because of volume conservation (incompressibility of nuclear matter); also the symmetry energy term (the second in the expression) and the pair energy term (the third) are not affected by a distortion, and hence, both don't appear in the liquid drop model of fission. Thus, the changes in the potential energy due to shape distortions are described in this model as the interplay between Coulomb and surface effects (fourth and fifth terms in 2.17). Consequently, the fission barrier can be considered as the energy necessary to distort the nucleus to a point where the decrease in Coulomb energy  $E_c$  becomes larger than the increase in surface energy  $E_s$ . For a small perturbation the Coulomb and the surface energies are given by (Bohr and Wheeler, 1939):

$$E_s = E_s^0(1 + \frac{2}{5}\alpha_2^2), \quad E_c = E_c^0(1 - \frac{1}{5}\alpha_2^2) \quad (2.18)$$

Here  $\alpha_2$  is the distortion parameter,  $E_s^0$  and  $E_c^0$  are the energies of unperturbed spheres. From these equations one can define the fissibility parameter as :

$$x = \frac{E_c^0}{2E_s^0} \quad (2.19)$$

For  $x$  less than unity, the drop will be stable to small distortions, for  $x$  larger than 1 there will be no potential energy to forbid the spontaneous fission of the drop. As said before, this model gives only a first orientation, in fact it predicts that for  $Z$  larger than 125 there will be no barrier. A more adequate description is the single particle model that includes the shell effects, the spin-orbit force and assumes a non spherical potential (see Strutinsky Hybrid Model [5] page 27–35).

The tunneling probability depends exponentially on the square root of the barrier height. For elements lighter than Thorium the barrier is so high and the penetrability so low that spontaneous fission has never been observed. However, for the heaviest elements it becomes a very prominent mode of decay, and the fact that elements heavier than those known do not exist in nature arises from the instability of these nuclei respect with to spontaneous fission.

The largest fraction of the available energy released in the fission goes into kinetic energy of the fragments. Empirically the total kinetic energy is proportional to  $Z^2/A^{\frac{1}{3}}$ , this can be qualitatively understood by assuming that the kinetic energy of the fragments is a result of the Coulomb repulsion of two spheres in contact:

$$V_c = \frac{Z_1 Z_2 e^2}{R_1 + R_2} \quad (2.20)$$

Considering a symmetric fission and using the relation  $R = r_0 A^{\frac{1}{3}}$ , one obtains:

$$V_c = \frac{Z^2 e^2}{8(\frac{1}{2})^{\frac{1}{3}} r_0 A^{\frac{1}{3}}} \quad (2.21)$$

In this calculation spherical fragments rather than deformed ones are assumed, hence, the observed kinetic energy deviates substantially from that expected. An improved empirical relation is obtained adding a constant term to the term proportional to  $Z^2/A^{\frac{1}{3}}$  as illustrated in Fig.2.6

Extensive measurements of the dependence of the kinetic energy on the mass of a fission fragment have been performed. The result of a similar experiment for spontaneous fission of  $^{252}\text{Cf}$  is illustrated in Figure 2.7; the maximum of the kinetic energy released to a fragment occurs at  $A \simeq 132$ . The average energies of the single fragments and their probability of emission are summarized in Tab.3.2.

The experimental data of the charge distribution of the fission fragments for the  $^{252}\text{Cf}$  are shown in Fig.2.8 and summarized in Tab.3.2. This data are taken after the prompt emission of neutrons in the fission process; for this reason the mass of the fragments in Fig.2.8 is called the post neutron mass.

The ionization density of the fission fragment is very large compared to  $\beta$ - or  $\alpha$ - particles, thus, the recombination is large. However, the number of free electrons produced is at least a factor 3 larger than for the other two types of source (see section 3).

A summary of the most important characteristics of  $^{252}_{98}\text{Cf}$  is listed in table 2.3.

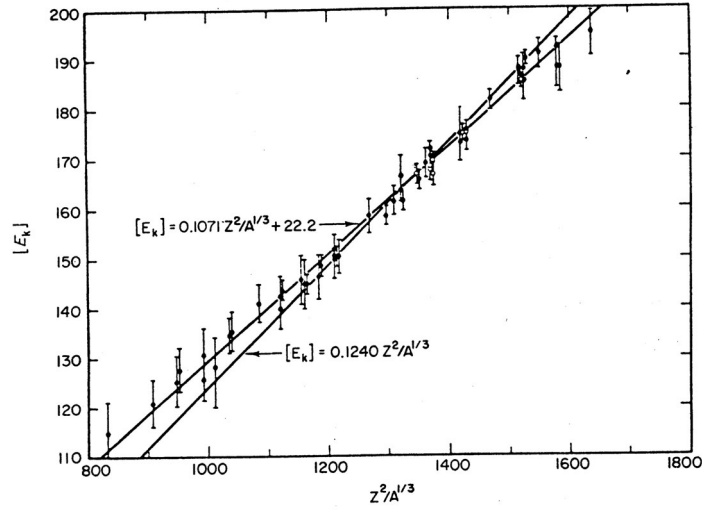


Figure 2.6: Dependence of the most probable kinetic energy of the fission fragments on  $Z^2/A^{1/3}$

Table 2.3: Important characteristics of  $^{252}_{98}\text{Cf}$

Decay mode	$\alpha$ 96.908%, SF 3.092%, $\beta$ stable
$\alpha$ energy (MeV)	6.1183, 6.0757, 5.9766, 5.8263, 5.516
Most probable total kinetic energy	185.5 MeV
Half life	2.646 years

### 2.2.2 The electronic stopping power of high velocity heavy ions

To apply the traditional stopping power theory discussed in section 2.1.3 to the fission fragments, one has to estimate the degree of ionization of the projectile. Bohr suggested that the ion can be considered to be stripped of the electrons, whose classical orbital velocity is less than the ion velocity. Using the Thomas–Fermi atom he showed that:

$$Z_i^* = Z_i^{1/3} v_i / v_o \quad (2.22)$$

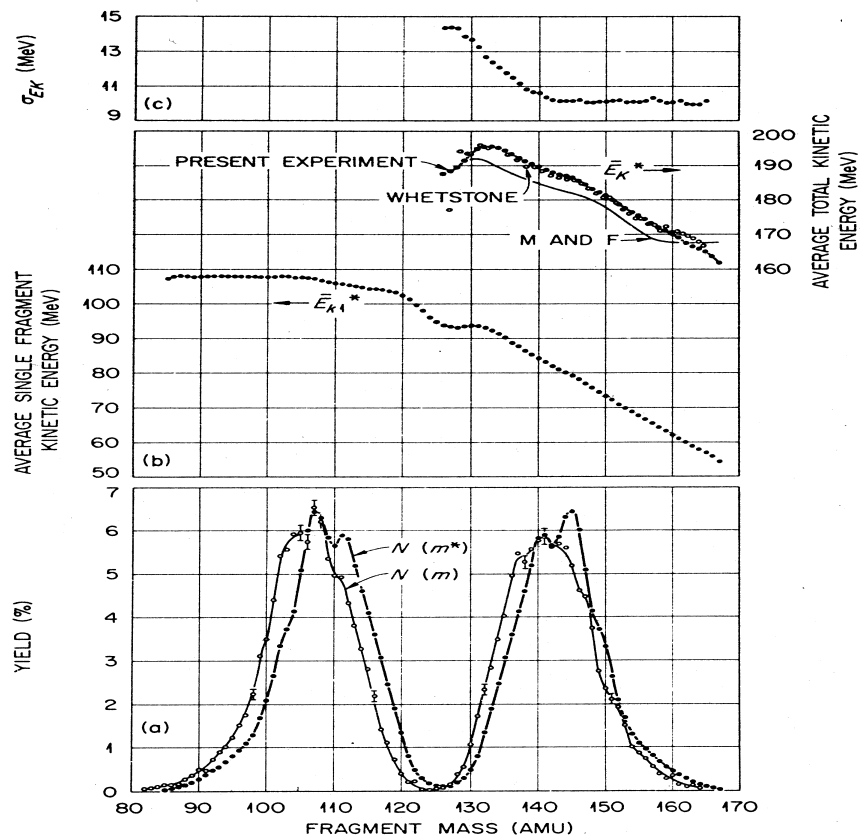


Figure 2.7: Spontaneous fission of  $^{252}\text{Cf}$

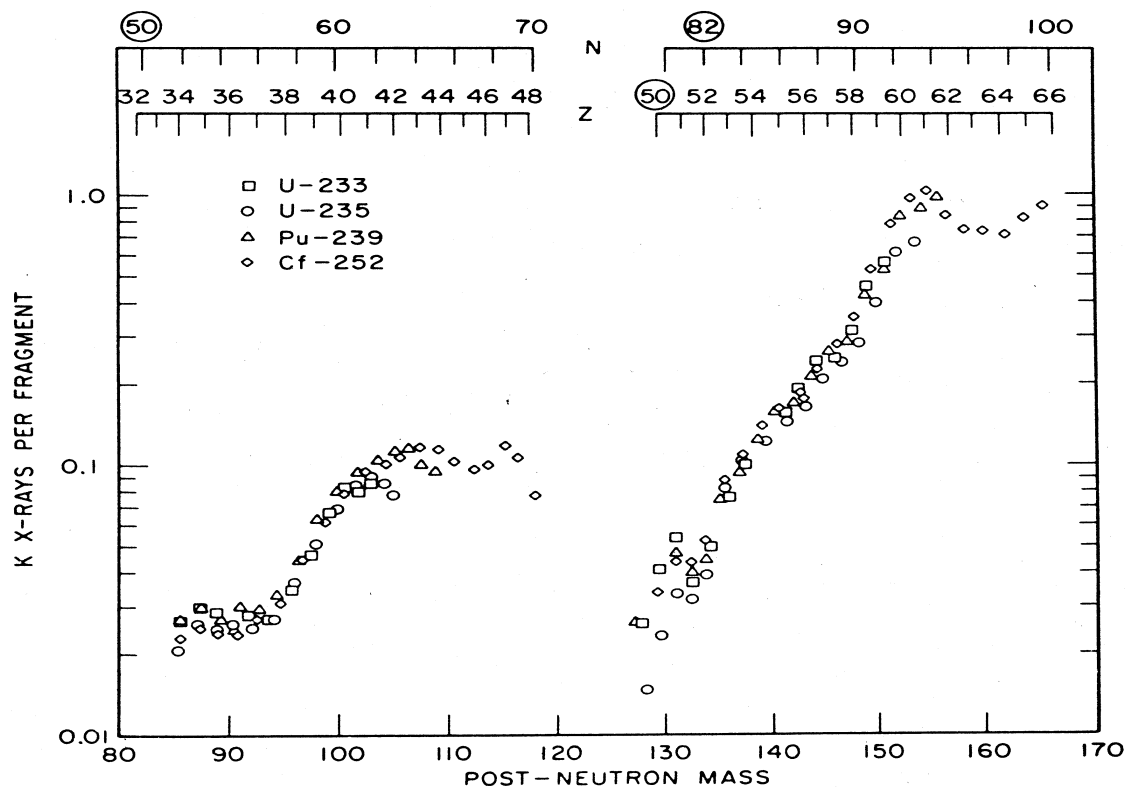


Figure 2.8: K x-rays per fragment emitted within 1 nsec after fission as a function of the post neutron mass for  $^{252}\text{Cf}$ . Approximate average proton and neutron numbers are given on the upper abscissa.

where  $Z_i^*$  the effective charge of the ion,  
 $Z_i$  the atomic number of the heavy ion,  
 $v_i$  the ion velocity,  
 $v_o$  the Bohr velocity ( $\sim 2.2 \cdot 10^8 \text{ cm/sec}$ ).

An extension of Bohrs relation fitted to experimental data was found by Northcliffe and is given by the expression:

$$Z_i^* = Z_i(1 - \exp[-0.92v_i/(v_o Z_i^{2/3})]) \quad (2.23)$$

Knowing the effective charge, one can use an empirical rule for the calculation of fast heavy ions in solids or liquids, which relates their stopping power to that of the equivalent proton stopping powers (see eq.(2.9)). This so called heavy-ion scaling rule has the form:

$$S_i = S_p(Z_i^*)^2 \quad (2.24)$$

where  $S_i$  and  $S_p$  are the stopping power of the ion and the proton. Fast ions means that their Fermi velocity  $v_F = \frac{\hbar}{m}(3\pi^2\rho)^{1/3}$  is smaller than their velocity  $v_1$ . In the case of the fragments of  $^{252}\text{Cf}$  the condition  $v_F < v_1$  is always satisfied.

### 2.2.3 The SRIM simulation

SRIM (Stopping power of ions in matter) is a collection of programs to calculate the stopping power and range of ions (10 eV - 2 GeV) in matter, using a quantum mechanical treatment of ion-atom collisions. This calculation is made very efficient by the use of statistical algorithms which allow the ion to make jumps between calculated collisions and then averaging the collision results over the intervening gap. During the collisions, the ion and atom have a screened Coulomb field, including exchange and correlation interactions between the overlapping electron shells. The ion has long range interactions creating electron excitations and plasmons within the target. These are described by including a description of the target's collective electronic structure and interatomic bond structure. The charge state of the ion within the target is described using the concept of effective charge (Eq. 2.23), which includes a velocity dependent charge state and long range screening due to the collective electron sea of the target. Table 3.2 summarizes the calculated

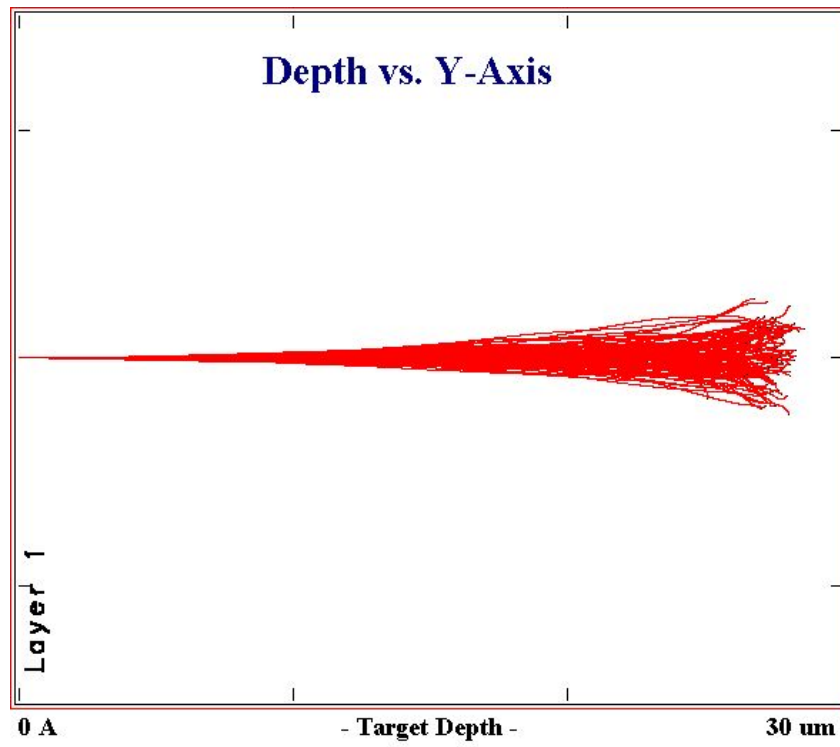


Figure 2.9: Ion distribution in LAr simulated with SRIM for a possible Sr(38) fragment of  $^{252}\text{Cf}$  with energy of 108 MeV.

range for the different fragments. The program gives also the stopping power as a function of the distance, so that the free electron density can be found, taking into account the recombination effect(see next chapter).

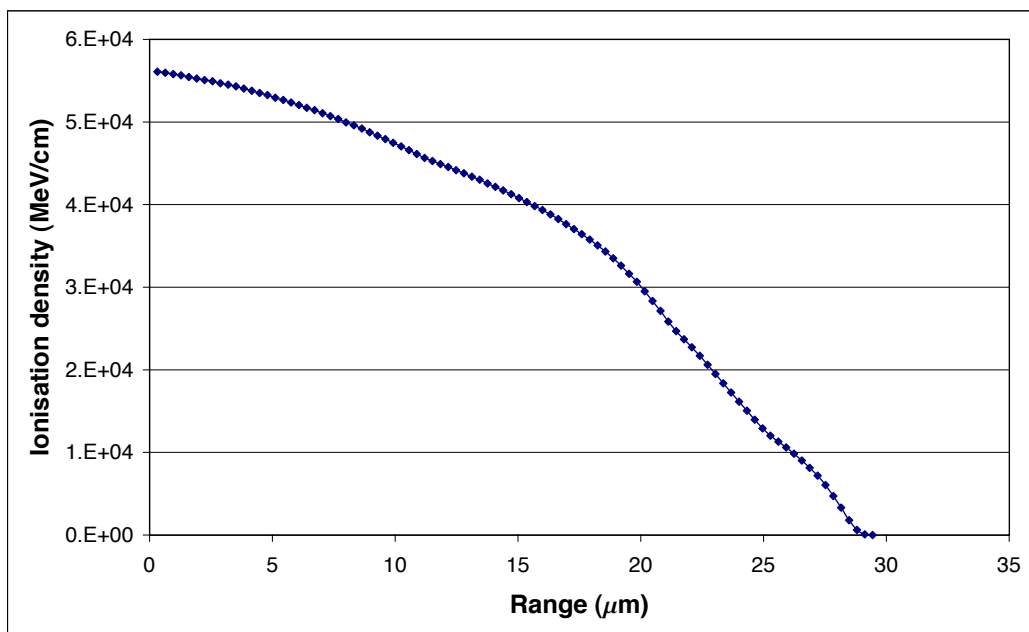


Figure 2.10: Ionization density simulated with SRIM for a Kr(36) ion

## Chapter 3

# Calculation of the number of free electrons and choice of the field configuration

### 3.1 The recombination effect

To calculate exactly the number of free electrons created by an ionizing particle one has to consider the recombination of  $e^-$ -ion pairs. If the ionization density is high, such as for  $\alpha$ -particles or ions, this effect cannot be neglected. A semiempirical equation is given by the Birks Model [7] which considers the strong dependence of the recombination on the electric field and on the ionization density. The number of free electrons after recombination is given by:

$$\frac{N}{N_0} = \frac{1}{N_0} \int_0^x \frac{\frac{dE}{dx} \cdot \frac{1}{w}}{1 + k_1(|\vec{E}|) \frac{dE}{dx} \cdot \frac{1}{\rho}} dx \quad (3.1)$$

where  $w = 23.6eV$  is the mean energy needed to produce an  $e^-$ -ion pair,  
 $\frac{dE}{dx}$  is the energy deposited by the particle,  
 $\rho = 1.4g/cm^3$  is the density of the LAr,  
 $|\vec{E}|$  is the E-field in the recombination region,  
 $k_1(|\vec{E}|)$  is the Birks factor,  
 $x$  is the range of the projecticle in LAr.

The Birks factor for LAr is only given for a field  $E = 500V/cm$  and is [7]:

$$k_1(500V/cm) = 0.1075g \cdot MeV^{-1} \cdot cm^{-2} \quad (3.2)$$

The dependence on the  $\vec{E}$  field can be calculated with the Box Model [8] with the assumption that the ion–electron pairs are spatially isolated and initially uniformly distributed in a box of a certain dimension. With this model the ratio of free electrons before and after the recombination is:

$$\frac{N}{N_0} = \frac{|\vec{E}|}{C} \ln\left(1 + \frac{C}{|\vec{E}|}\right) \quad (3.3)$$

Here  $|\vec{E}|$  is the strength of the electric field in the recombination region. The factor  $C$  depends on the ionization density distribution, but is independent of  $|\vec{E}|$ . Thus, with equation (3.1) its value for each particle can be determined using (3.2). Knowing the  $C$ -values the Birks factor can be evaluated for different fields  $\vec{E}$  and consequently the number of electrons after recombination can be evaluated for different E-fields.

## 3.2 The Beta source

### 3.2.1 Expected number of free electrons

If we assume the ionization density to be constant along the track of the positron, we can calculate  $C$  and the Birks factor as explained in the previous section, the results are given below:

For positrons and fields in the range of  $|\vec{E}| \simeq 5\text{--}10\text{ kV/cm}$  the ionization density and the Birks factor are so small that the recombination effect can be neglected (see 3.1). Knowing the mean energy necessary to obtain an  $e^-$ -ion pair one can simply calculate the number of electrons produced by the ionizing positron as follows:

$$N = \frac{E}{w} \quad (3.4)$$

where  $N$  is the number of free electrons

$w = 23.6\text{eV}$  is the mean energy necessary to produce an  $\text{e}^-$ -ion pair in LAr

$E$  is the deposited energy of the positron

The total initial charge that we expect to measure is:

$$Q_i = 1.6022 \cdot 10^{-19} C \cdot N \quad (3.5)$$

This charge passing through the preamplifier/amplifier, it will be transformed into a measurable voltage (see also section 5.3.1.

With Eqs. (1.1), (3.5) and knowing the deposited energy of the positron, which can be extracted using the values of table 2.2, we find:

Table 3.1: Number of free electrons and charge created by positrons in LAr

Initial $e^+$ kinetic energy (MeV)	Number of free electrons	Created charge $Q_i$ (fC)
0.1	4200	0.7
0.25	10600	1.7
0.5	21200	3.4
0.75	31800	5.1
1	42400	6.8
1.25	52900	8.5
1.5	63600	10.1
1.75	74200	11.9
1.83	77500	12.4

### 3.2.2 The electric field

The free electrons created by the ionizing positron drift from the cathode to the grid and finally to the anode. The cathode is a halfsphere of 3 mm diameter and 10 mm long, as shown in Fig.4.1. The grid and the anode are discs of 93 mm diameter. The resulting electric field is sketched in Fig.3.1 and can be calculated with the method of (virtual) images:

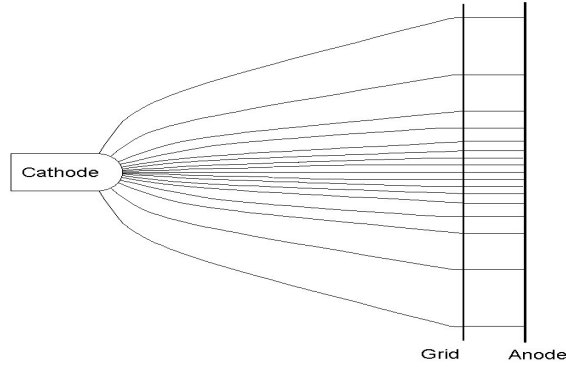


Figure 3.1: Field generated by the three electrodes for the  $^{22}\text{Na}$  source

$$E(\vec{r}) = \frac{V_c \cdot R}{\vec{r}^2} \frac{\vec{r}}{|\vec{r}|} + \frac{V_a \cdot R}{(\vec{r} - \vec{d})^2} \frac{\vec{r} - \vec{d}}{|\vec{r} - \vec{d}|} \quad (3.6)$$

where  $E(\vec{r})$  is the electric field at  $\vec{r}$ ,  
 $V_c$  is the voltage applied at the image charge,  
 $V_a$  is the voltage applied at the anode,  
 $\vec{d}$  is the position vector of the anode with respect to the cathode,  
 $|\vec{d}|=2$  times the distance cathode-grid,  
 $\vec{r}$  is the position relative to the source.

The advantage of such a geometry, compared for example to the plate capacitor purity monitor of the ATLAS experiment (see Figure. 1.2), is that the electron drift time is increased because the field isn't constant. In fact in the region near the grid we have field strengths of only a few V/cm. This allows us to measure the exponential decay of the charge of free electrons more precisely, even for long life times of the electrons.

### 3.3 The spontaneous fission source

#### 3.3.1 Expected number of free electrons

In the case of the ions emitted by the  $^{252}\text{Cf}$  the ionization density is big, thus, the quenching becomes important. To estimate the number of free electrons after the recombination one has to calculate the Birks factor by substituting  $dE/dx$  in 3.1 with the values calculated with the SRIM program. The results are listed in Tab.3.2.

Table 3.2: Number of free electrons produced by the fission fragments and their range in LAr

Z	A	Probability	E/MeV	free $e^-$	Range/ $\mu m$	C·cm/kV
36	90	0.5	108	132000	29.44	14700
38	95	1.3	108	130000	28.80	14980
40	100	3.5	108	125000	27.60	15600
42	105	6	108	124000	27.30	15650
44	110	5	107	122000	27.00	16180
46	115	3	105	118000	26.04	16760
48	120	0.4	105	119000	26.56	16620
50	130	1	93	113000	24.96	14790
52	135	4	90	113000	25.20	14790
54	140	5.8	85	104000	24.00	15490
56	145	5.5	79	104000	23.00	16450
58	150	2.3	72	100000	21.75	20600
60	155	0.9	67	93000	20.30	22400
62	160	0.2	62	88000	18.88	23900

#### 3.3.2 The electric field

The electric field is generated by two spheres at a distance  $d$  (Fig.3.2). Such a geometry has the advantage of reducing the recombination effect of electron-ion pairs because near the surface of the cathode the electric field is very high (about 40kV/cm for a high voltage of 1kV and a radius of 0.25mm). This electric field configuration permits also long drift times because in the

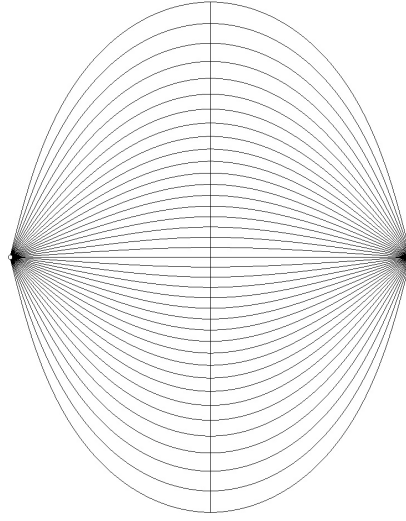


Figure 3.2: Dipol field generated by two sphere at a distance d

middle region the strength of the field is only a few V/cm.  $\vec{E}$  is calculated as a superposition of Coulomb fields as follows:

$$E(\vec{r}) = \frac{V_c \cdot R}{\vec{r}^2} \frac{\vec{r}}{|\vec{r}|} + \frac{V_a \cdot R}{(\vec{r} - \vec{d})^2} \frac{\vec{r} - \vec{d}}{|\vec{r} - \vec{d}|} \quad (3.7)$$

where  $E(\vec{r})$  is the electric field at  $\vec{r}$ ,  
 $V_c$  is the voltage applied at the cathode,  
 $V_a$  is the voltage applied at the anode,  
 $\vec{d}$  is the position vector of the anode with respect to the cathode,  
 $\vec{r}$  is the position relative to the source.

## Chapter 4

# Monte Carlo simulation of the drift time and the signal width

A Monte Carlo simulation has been performed in order to study the effects of the diffusion and the inhomogeneous electric field on the cloud of starting electrons for both sources. Electrons created by the ionizing particle which start near the surface and those starting at the end of the range follow different field lines and, consequently, the time it takes them to reach the anode is different. Clearly, the emission angle of the ionizing particle (see Fig.4.1) plays an important role and has been taken into account.

The voltage between electrodes and the diameter of the spherical electrodes have been optimized to obtain measurable pulses with widths of less than  $100\mu s$  and with drift times of the order of  $1ms$ .

### 4.1 The drift velocity

An empirical equation that describes the drift velocity in liquid Argon at  $90.371\text{ K}$  as a function of the applied electrical field has been found by ([11]) and is:

$$v_d(|\vec{E}|) = (P_1|\vec{E}| \ln(1 + \frac{P_2}{|\vec{E}|}) + P_3|\vec{E}|^{P_4}) \quad (4.1)$$

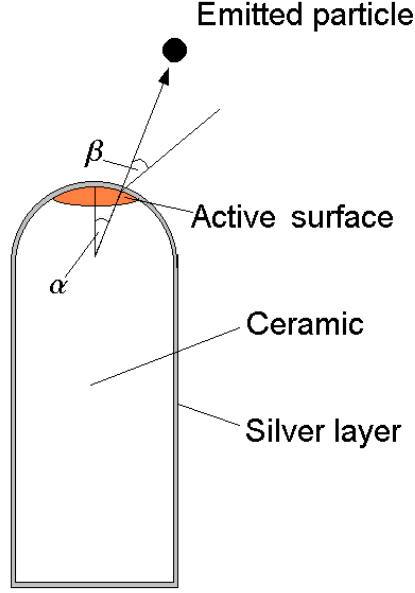


Figure 4.1: Angles of emission of the ionizing particle

where  $v_d$  is the drift velocity in  $\text{mm}/\mu\text{s}$ ,  
 $|\vec{E}|$  is the electric field,  
 $P_1 = 0.141 \pm 0.023 (\text{kV}/\text{cm})^{-1}$ ,  
 $P_2 = 12.4 \pm 2.7 (\text{kV}/\text{cm})$ ,  
 $P_3 = 1.627 \pm 0.078 (\text{kV}/\text{cm})$ ,  
 $P_4 = 0.317 \pm 0.021$ .

The measurements leading to this formula have been performed for electric field strengths in the range of  $0.5 \text{kV}/\text{cm} \leq |\vec{E}| \leq 12.6 \text{kV}/\text{cm}$ , thus, for the region near the grid where  $|\vec{E}|$  is only few  $\text{V}/\text{cm}$ , the relation has to be verified.

#### 4.1.1 The diffusion

A localized electron cloud diffuses with time through multiple scattering and adopts a Gaussian form around the center point with a time dependent width (root mean square):

$$\sigma = \sqrt{2Dt} \quad (4.2)$$

where  $\sigma$  is the Gaussian width,  
 $D = 5\text{cm}^2/\text{s}$  is the diffusion coefficient for LAr,  
 $t$  is the time in seconds.

The diffusion coefficient for LAr is very small compared to that of gas, however, if the drift time is long, this effect becomes important and has to be considered. From the grid to the anode the field is constant so that only the diffusion contributes to the time spread of the electron cloud in this region; however, the drift time is so small that in the simulation this influence has been neglected. An example of 1000 electron which start at the same point on the surface of the cathode with the field geometry of the beta source is plotted in Fig.4.2.

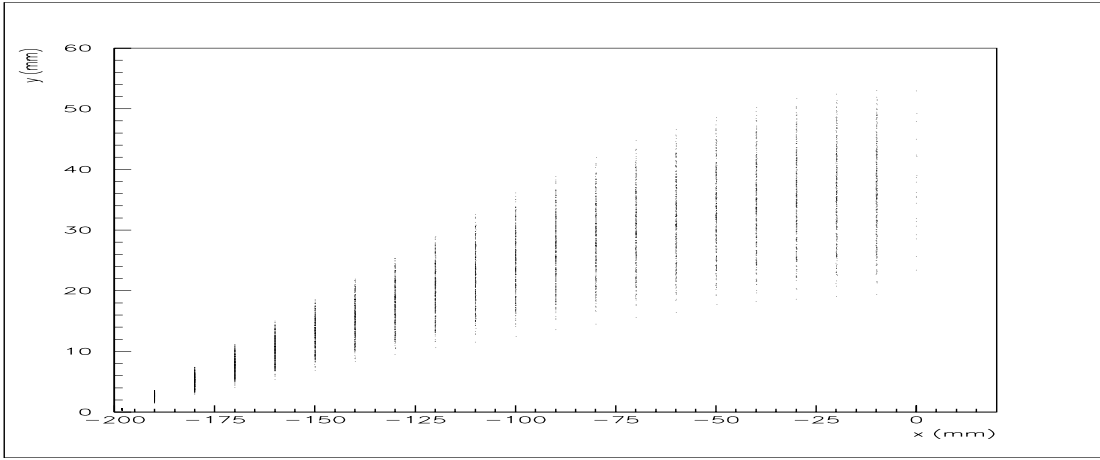


Figure 4.2: Diffusion of 1000 electrons started at the surface with  $\alpha = 10^\circ$  and  $\beta = 90^\circ$

## 4.2 Results

### 4.2.1 The $^{22}\text{Na}$ -cell

In the simulation a simplified geometry is used with only two electrodes (the cathode and the grid). In fact, the time it takes the electrons to drift from the grid to the anode and the diffusion during this drift (5mm) has been neglected

because in this region the field is constant and very high (0.5kV/cm), thus, the drift time is very short. The result of the simulation is that with a half-sphere radius of 1.5 mm, for  $\alpha < 10^\circ$  and  $\beta = 90^\circ$  (to take into account the worst case, see Fig.4.1) and an applied high voltage difference cathode-grid of 2kV, the pulse has the desired width and the drift time is about  $840\mu\text{s}$  (see Fig.4.3). These two parameters can be changed varying the distance between the electrodes and/or the applied high voltage.

Radius of the source	1.5mm
Distance	cathode-grid 200mm
High voltage	cathode -2kV grid 0V

#### 4.2.2 The $^{252}\text{Cf}$ -cell

As mentioned before, the simulation allows to optimize the radius of the sphere, the applied high voltage and to determine the cut on the angle  $\alpha$ . Since the recombination in the case of a  $^{252}\text{Cf}$ -cell plays an important role the radius has to be of the order of  $R=0.25\text{mm}$ , so that in the recombination region the field is very high. Indeed, as explained in section 3.1, the recombination decreases with increasing  $|\vec{E}|$ .

Radius of the spheres	0.25mm
Distance	cathode-anode 200mm
High Voltage	cathode -1kV anode +1kV

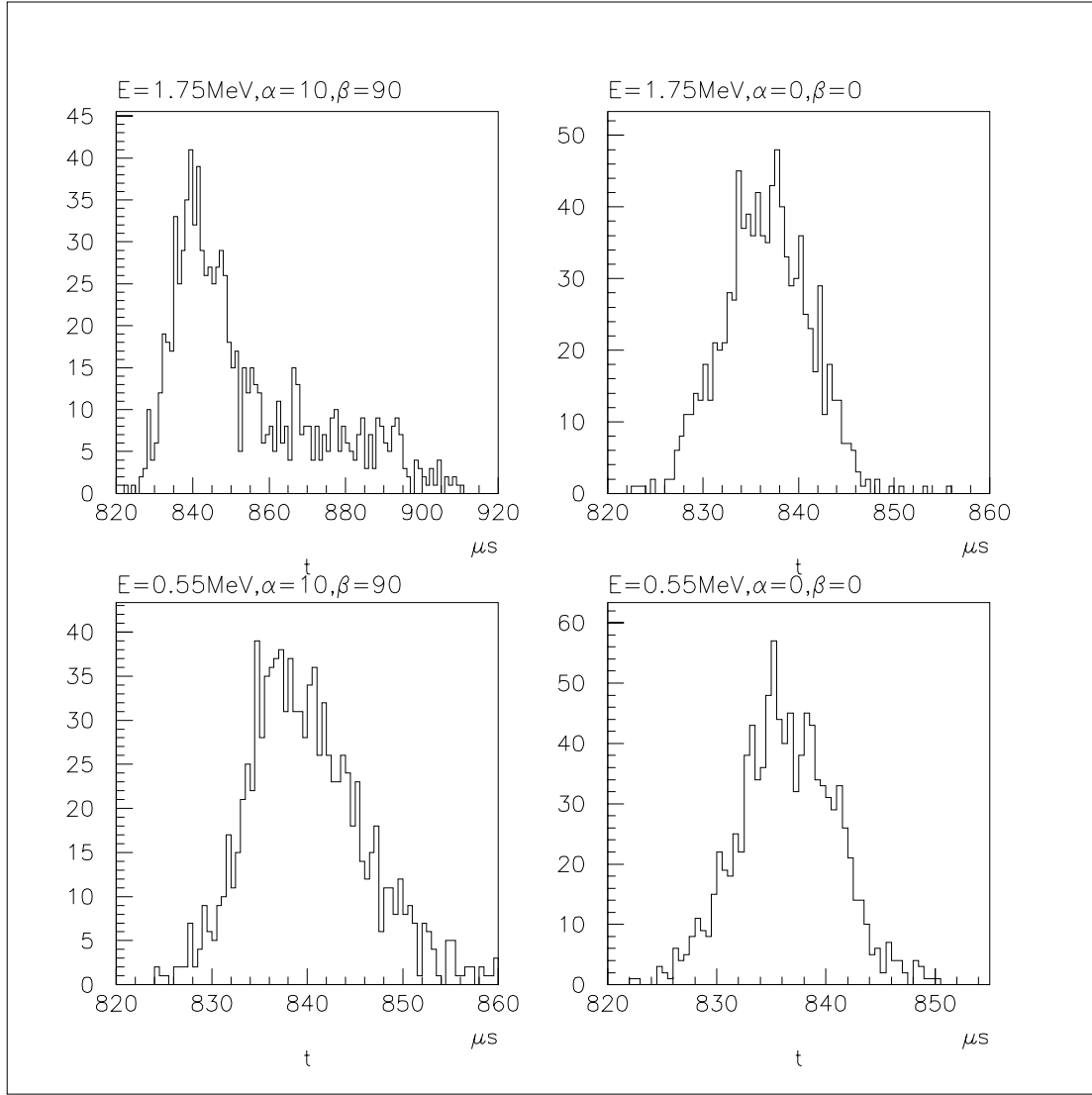


Figure 4.3: MC simulation of 930 electrons produced by the ionizing positron. The position of the starting positron on the cathode is defined by  $\alpha$  and its direction by  $\beta$  (see Fig.4.1). The high voltage applied to the cathode is 2kV, the grid is at 0V and the distance between them is 200mm

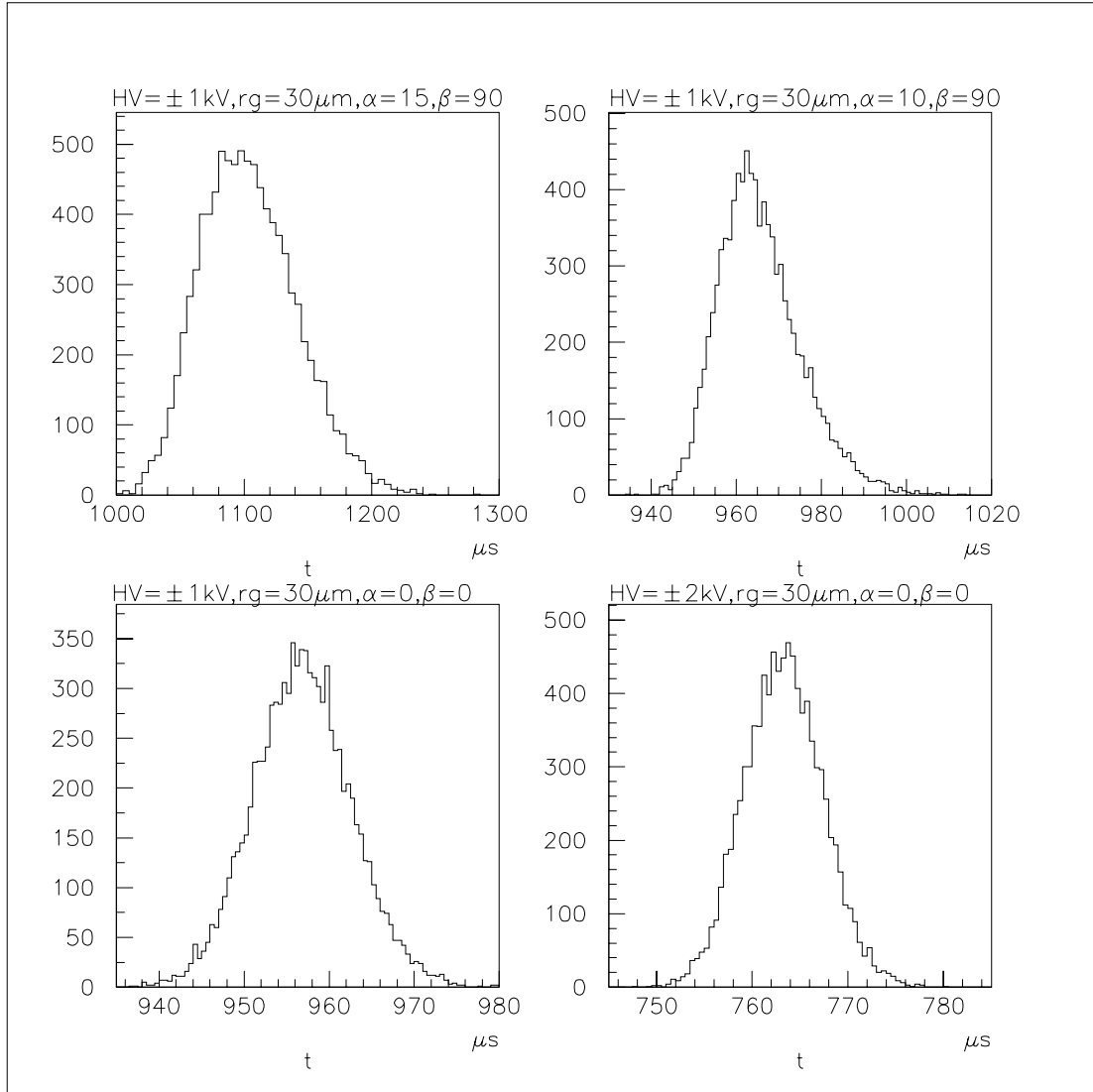


Figure 4.4: MC simulation of 9000 electrons produced by a fission fragment. The distance between the spheres is 200mm and their radius is 0.25mm

# Chapter 5

## Experimental Set-up

### 5.1 Mechanics of the purity monitor

#### 5.1.1 The $^{22}\text{Na}$ -cell

Figure 5.4 shows a schematic view and a photograph of the monitor, which is surrounded by a stainless steel cylinder of 104 (108) mm internal (external) diameter. The cylinder is covered at the bottom and at the top by 10 mm thick steel plates with holes in order to let the LAr flow in at the bottom and to let bubbles escape at the top. The cathode-anode distance can be varied from 0–150 mm. The grid and the anode are held together by three Dehoplast (polyethylene) rods to insulate them from each other and from the outer cylinder. The distance and the voltage between the three electrodes has to be adjusted so that the field ratio  $E_A/E_B$  is at least 1/3 for optimal transparency [6]. The grid has a pitch of 5 mm; its function is to electrically shield the anode from the starting electrons and to pick-up an induced signal when the electrons are passing through it. It has been made of Molybdenum with laser extrusion. The main parameters of the monitor are summarized in the table 5.1. All the materials used have been chosen in order to minimize the pollution of the LAr (they don't outgas too much) and they have good properties at the temperature of LAr (87.5K). The cathode is a half-sphere of 1.5 mm radius. The radioactive source is deposited on its surface as explained in the next section.

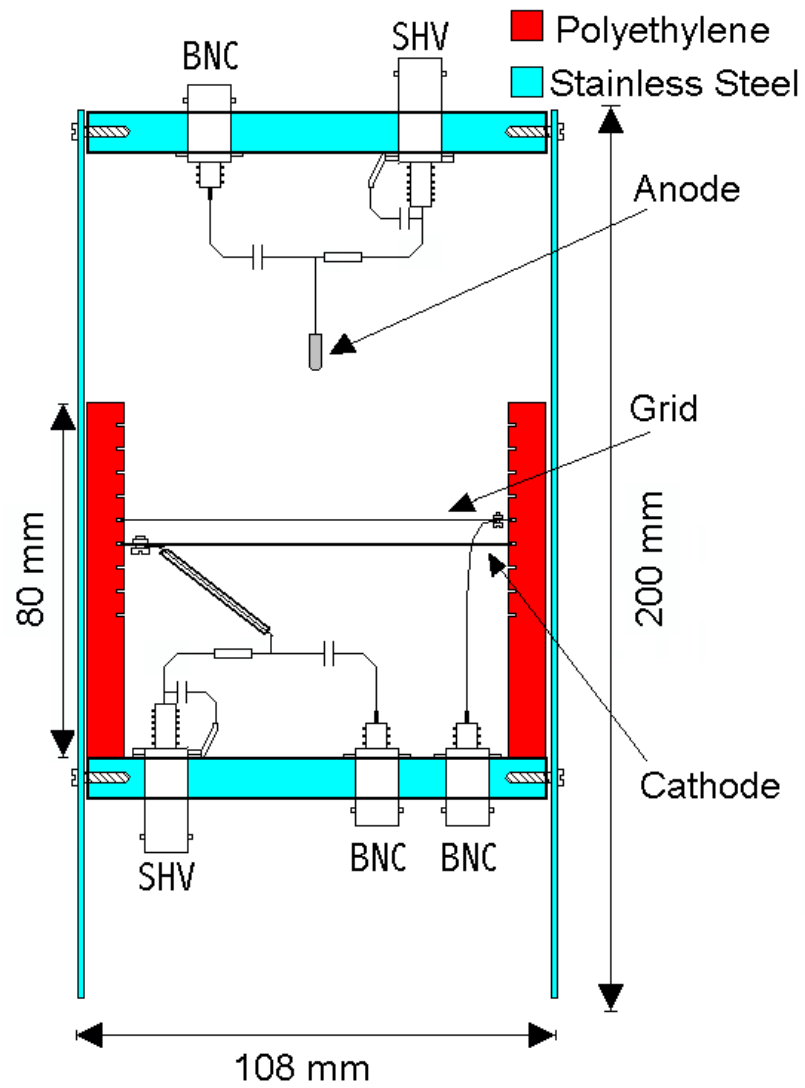


Figure 5.1: Schematic view of the purity monitor

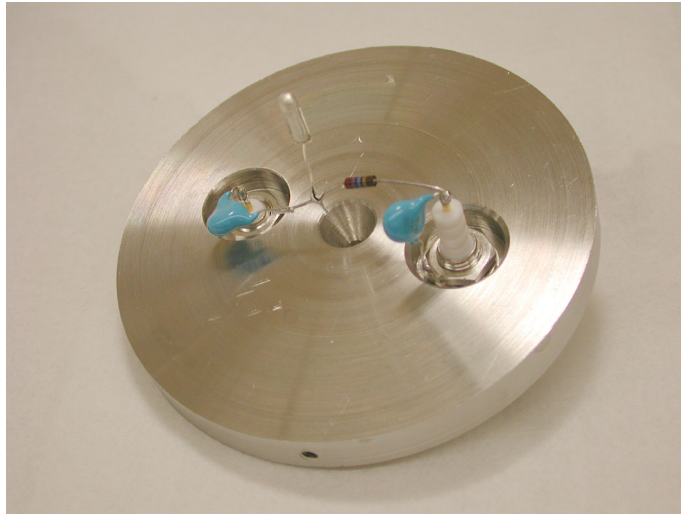


Figure 5.2: Photograph of the source and its holder

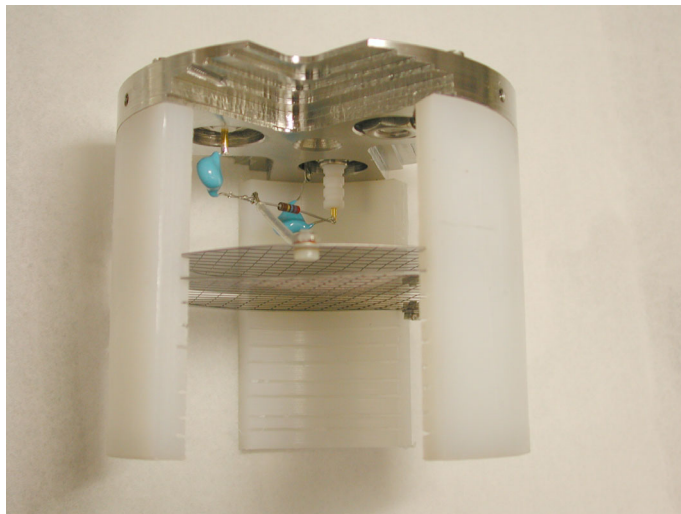


Figure 5.3: Photograph of the anode, the grid and its holder

Table 5.1: The main parameters of the monitor

	Shape	Dimension	Material	Applied High Voltage
Cathode	Half sphere	3mm diameter	Poros ceramic	-1.5kV
Anode	Disc	93mm diameter 0.5mm thick	Stainless steel	+1.5kV
Grid	Disc	93mm diameter, 5mm pitch, 0.15mm thick	Molybdenum	0V

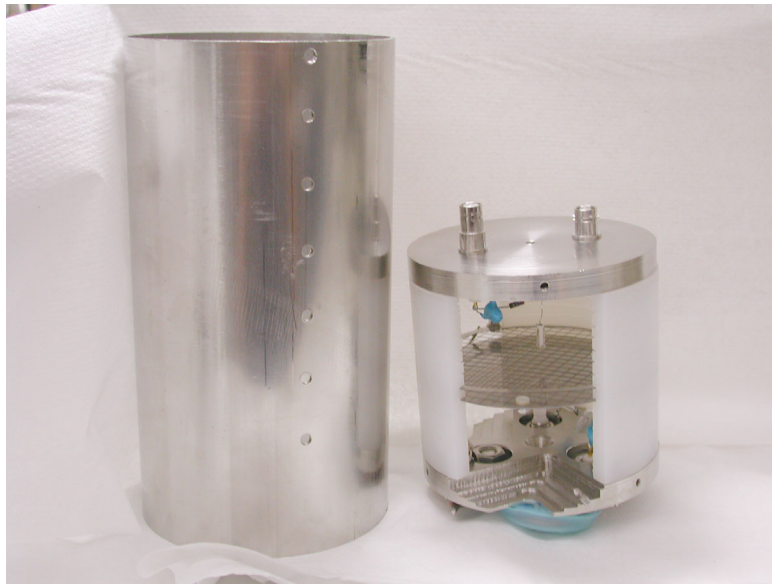


Figure 5.4: Photograph of the purity monitor

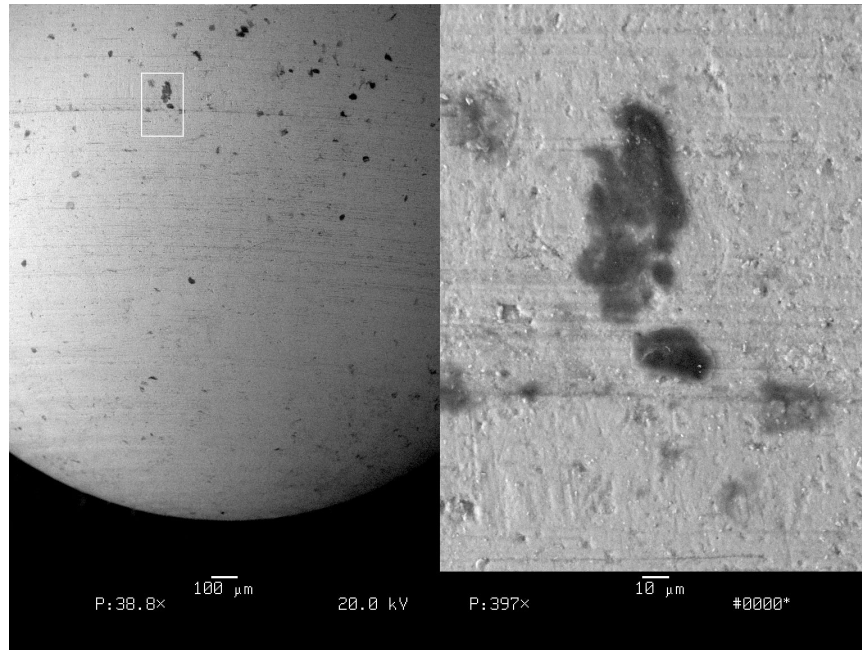


Figure 5.5: Photograph of the ceramic rod from the electron microscope. The black spots are the pores of the ceramic.

### 5.1.2 Deposition of the source on the cathode

To deposit the source to the half sphere of 1.5 mm radius (cathode) the principle of ion exchange was used. A porous ceramic has been chosen as a holder in order to increase the surface of exchange. Thus, immerses the piece in a solution containing  $^{22}\text{Na}$ , it is possible to obtain the desired radioactive source.

The ceramic is  $\text{ZrO}_2 + \text{Y}_2\text{O}_3 (3\text{mol}\%)$  with impurities  $\text{K}_2\text{O}$ ,  $\text{Na}_2\text{O}$ ,  $\text{Al}_2\text{O}_3$ ,  $\text{SiO}_2$  smaller than 1% and a pore size of about 7nm (see Fig.5.5); it has been furnished by the Department of Nonmetallic Materials, ETH Zürich, Switzerland.

The radioactive isotope has been purchased at AEA Technology GmbH, D-38110 Braunschweig, Germany; the  $^{22}\text{Na}$  source with a total activity of 200kBq is diluted in a solution containing 0.1 molar of HCL.

The activity deposited on the ceramics depends on the immersion time: 1 hour of immersion corresponds to about 5Bq. For the tested monitor the activity is  $2500\text{Bq}/10\text{cm}^2$ , it has to be high because, as mentioned in sec.2.1.3, the branching fraction of the positrons an end point energy spectrum of

1.83MeV is only 0.06%.

The ceramic piece has been covered with silver foils to make it conductive, permitting a voltage to be applied, as explained in section 3.2.2. This has been performed by Mr. Scherrer at the EHTZ. In order to suppress pile up of the signals, the silver foil is 0.4mm thick, thus, the positrons from the spectrum with end point energy 0.543MeV is cut off. This has been calculated using the tables of the ICRU report [2] in the same manner of sec.2.1.2. The positron energies of the spectra with end point energy of 1.83MeV are reduced by about 0.4 MeV by the silver foil, consequently, the number of electrons created by ionization is lower than that calculated in sec.3. This will be considered later in the measurements.

To eliminate the water that the ceramic has absorbed from the solution and from the humidity in the air, which can cause a rupture of the piece if it is cooled in LAr, it has been heated for 70 minutes to 130 degrees, before the silver foils have been mounted.

## 5.2 The LAr filling procedure

Fig.5.6 shows the set-up used to test the purity monitor in LAr. In order to pollute the LAr as little as possible during the filling phase, the following procedure was followed:

1. Before filling the glass dewar with LAr the whole set-up was flushed with Argon gas from the LAr dewar. At first the set-up was pumped (with valve B closed) to a vacuum of about  $10^{-3}$  mbar. The reached pressure was limited by valve B on the LAr dewar, which is not completely vacuum tight. To fill the set-up with Ar gas, valve A was closed and valve B slowly opened, until the pressure in the set-up reached the vapor pressure of 1.7 bar of the LAr dewar (defined by the overpressure valve on the LAr dewar). The pumping and flushing with LAr was repeated twice.
2. To fill the glass dewar with LAr, the set-up was first evacuated again and filled with Ar gas (1.7 bar) one more time. Next, the pump was disconnected and both valves opened. After about five minutes the purity monitor in the glass dewar was completely covered by LAr. The valve

A was then closed, but valve B kept open to keep the Ar pressure in the set-up at the pressure of the LAr dewar during the measurements.

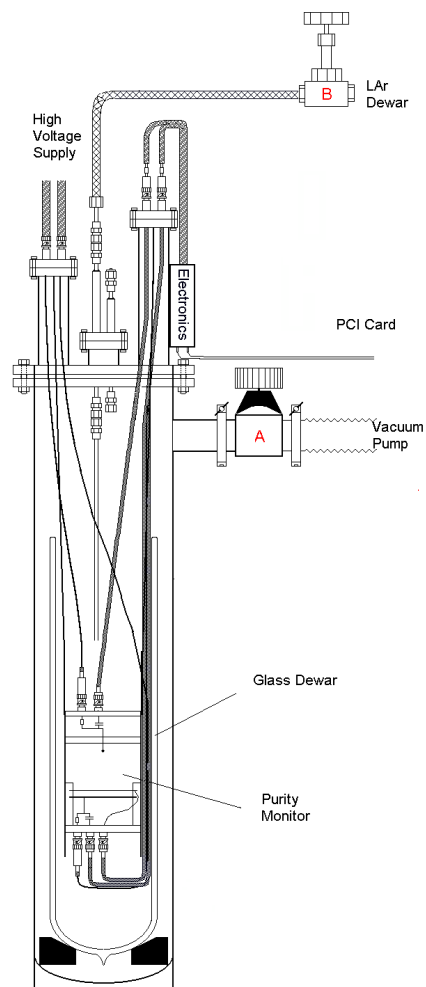


Figure 5.6: Schematic view of the filling set up

## 5.3 Electronics

The electronics to measure the electron pulses from the anode and the cathode is shown in figure 5.7. It operates at room temperature outside the test set-up and has three input channels: A is for the signal of the cathode, B is that of the anode and TEST is the input for the calibration. For channel A and B the electronics is composed of a preamplifier, two active band pass filters and an offset coupled with an amplifier which permits to adapt the output in the  $\pm 1V$  range of the PCI-card.

### 5.3.1 The preamplifier

The preamplifier is connected to the electrode with two 1,40m long coaxial cable through a 1000pF capacitor and a 27M $\Omega$  resistor, which protects it and acts as a band pass filter (see Fig.5.8). The charge, (created by the ionizing particle) passing through it is transformed in a measurable voltage. The preamplifier are of the type used in the ICARUS experiment [7] and have a sensivity of 0.92mV/10<sup>4</sup>e<sup>-</sup> [4]. The voltage supply is set at +12 and -5.

### 5.3.2 The active band pass filters

The filters were tuned in order to maximize the signal-to-noise ratio [12]. They are composed of a low band and a high frequency filter coupled with an amplifier, as shown in Fig.5.9, so that only the frequencies of the signal are amplified and those of the noise are suppressed. To determine the values of the capacitors and the resistors a simulation has been performed [4].

As one can see in Fig.5.7 the two filters are cascaded, thus, the resulting Bode Diagram is of the form shown in Fig.5.10 with the advantage of having a flatter curve on the top and consequently a larger bandwidth for the signal that will be amplified. Another benefit is that the slope is steeper, 40dB per decade instead of 20dB for a single stage, cutting off efficiently the low and high frequency noise. The maximal total gain is 100 at 100kHz.

The Op-Amp used are TLC072 from Texas Instruments; the noise for a frequency of 1kHz is 7 nV/ $\sqrt{Hz}$ , the open loop voltage gain  $R_{load} = \infty$  is 100dB and the gain bandwidth product is 10MHz.

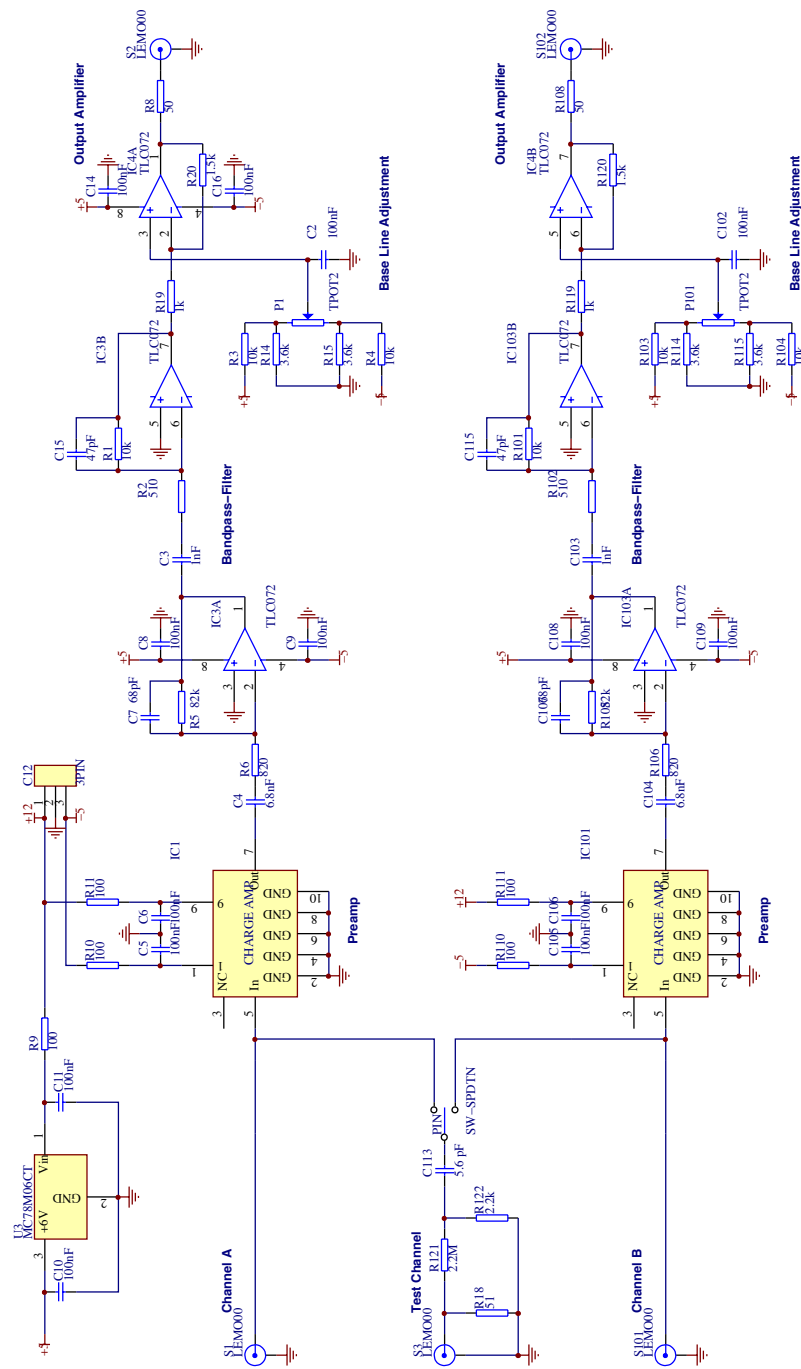


Figure 5.7: Electronic circuit

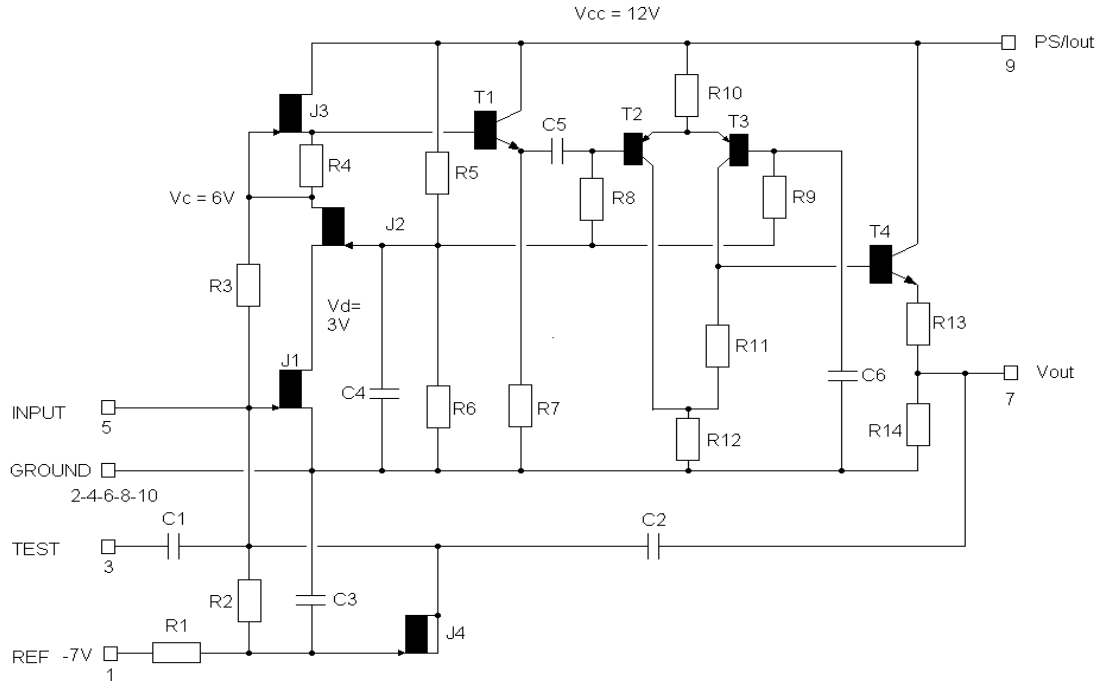


Figure 5.8: Circuit of the preamplifier

### 5.3.3 The offset and the $\pm 1V$ adaptor

Finally the pulses are amplified 1.5 times by the output amplifier stage of the circuit sketched in Fig.5.7. The resistors and the offset have been chosen so that the signal is optimally adapted to the  $\pm 1V$  range of the PC card, thus, the resolution is maximized.

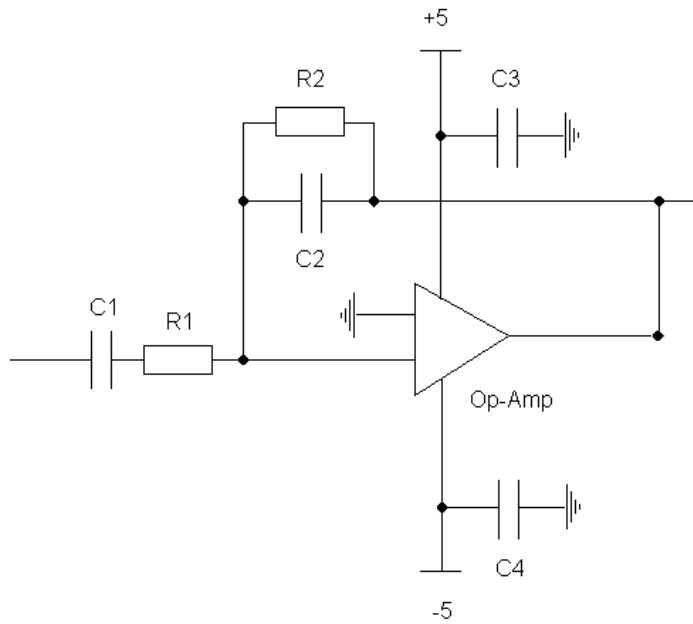


Figure 5.9: Scheme of the filters

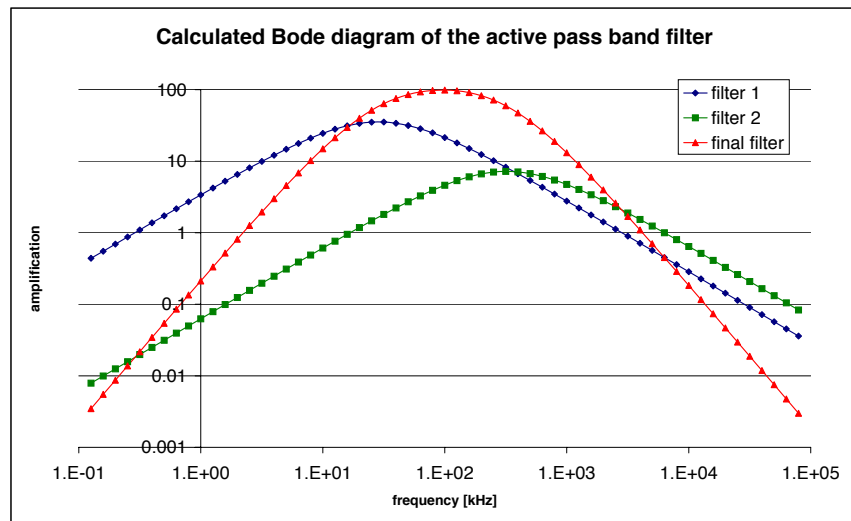


Figure 5.10: Frequency response of the filters

### 5.3.4 Test channel

The total gain is dependent on the signal width [12] so that a calibration

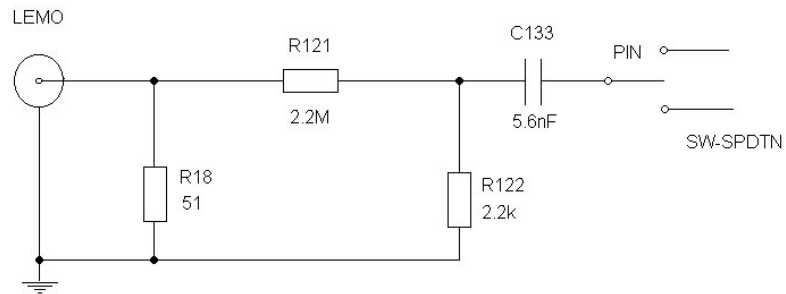


Figure 5.11: Scheme of the test channel

# Chapter 6

## Measurements

### 6.1 Data Acquisition and Analysis

The data were collected with an AD/DC PCI card (see table 6.1 for the main characteristics) and then analyzed offline with a LABVIEW program running on WINDOWS 95. The analysis is performed as follows:

- the stored outputs of the calibration (see section 5.3.4) are compared by the program with the real signals and then an algorithm chooses the best fit with the method of least mean squares so that the corrected height can be found;
- knowing the ratio between the anode and the cathode charge and their time separation, LABVIEW calculates the mean life of electrons in LAr with equation 1.2.

For the data taking the trigger is at the signal of the anode, this is efficient because not all the starting electron clouds from the cathode reach the anode. During the calibration an external trigger from the pulse generator is used.

The card has a maximal sample rate of 20MHz which has been used in our measurements. The input range has been set to  $\pm 1V$  for an optimal resolution.

Table 6.1: Main characteristics of the PCI card from Computer Boards INC.

Card type	PCI-DAS4020/12
Resolution	12 bits
Number of channels	4 single ended, 1 A/D per channel
Programmable ranges	$\pm 5V$ , $\pm 1V$
Coupling	DC
A/D conversion time	40ns
Input bandwidth	17MHz
Maximum sample rates	single and two channel 20MHz continuous; four channel 10Mhz continuous, 20MHz for 32k samples
Minimum sample rate	1kHz
Input Impedance	$50\Omega$ or $1.5M\Omega$
Maximal input voltage	$\pm 12V$
Trigger modes	A/D and/or gate Pre and post trigger

## 6.2 Measurements

During the measurements the distance cathode-grid, the distance grid-anode and the voltage of the grid were constant, the following table gives the values of these parameters.

Distance	cathode-grid 10mm grid-anode 5mm
High voltage	grid 0V

The high voltage at the electrodes and the trigger mode have been varied. In this chapter the measurements are presented in two sections: events triggered on the cathode and on the anode signal. Each measurement contains 1000 events and the total measurement time is about four hours. Table 6.2 summarizes the measurement conditions and Fig.6.1 shows an event.

Table 6.2: Measurements parameters

	Number of events	Triggered on	Trigger level (channels)	Cathode HV (kV)	Anode HV (kV)	Figure
1	1000	Cathode	1710	-1.5	+2.5	6.2
2	1000	Cathode	1710	-1.5	0	6.3
3	1000	Cathode	1710	-2.5	+2.5	6.4
4	1000	Cathode	1710	-2.5	0	6.5
5	1000	Anode	1010	-2.5	+2.5	6.6
6	1000	Anode	1010	-1.5	+1.5	6.7

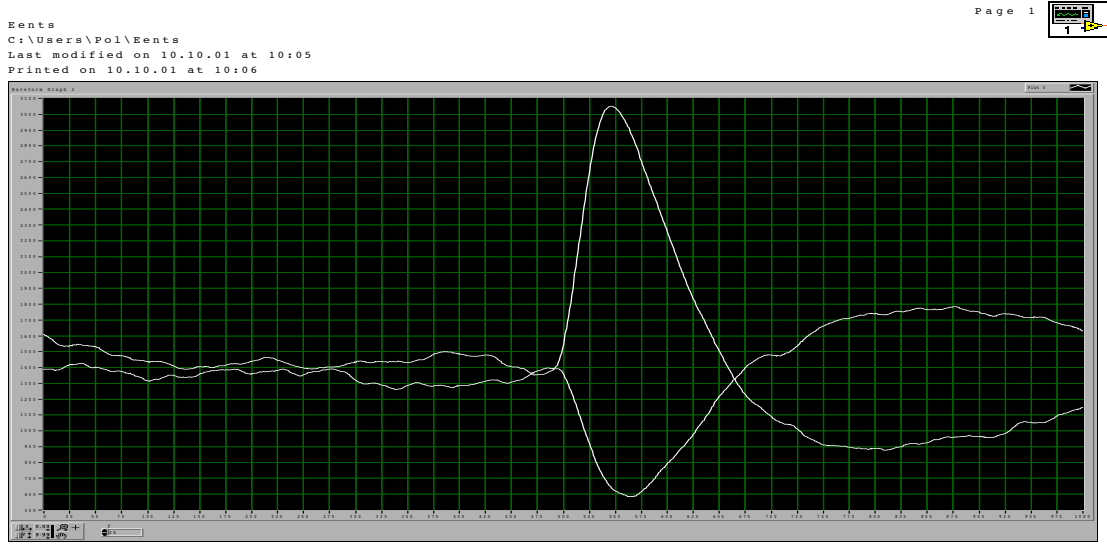


Figure 6.1: Single event measured with a high voltage of -1.5kV and +2.5kV. The horizontal scale is 25 ns per division and the vertical 50mV per div.

### 6.2.1 Trigger at the cathode

The trigger threshold was set to 1710 channels of the PC card; the results depend on the high voltage applied to the cathode.

### Cathode high voltage $-1.5\text{kV}$

In Figs. 6.2 and 6.3 a superposition of 1000 events is shown, this has been done to average out the noise. The positive pulse is the sum of the signals from the cathode, the negative one is the induced signal of the cathode to the anode. In fact the cathode-grid distance of 10mm is very small in comparison with the grid pitch of 5mm, so that the grid did not completely shield the anode from the induced signals. This distance has been chosen because the LAr was not pure enough to allow long drift times. No events with both pulses, the cathode signal and the delayed anode signal, were observed. This is probably due to the fact that the distance between the two electrodes is too large, thus, most starting electrons are captured during the drift by the LAr impurities, so that no anode pulse is detected.

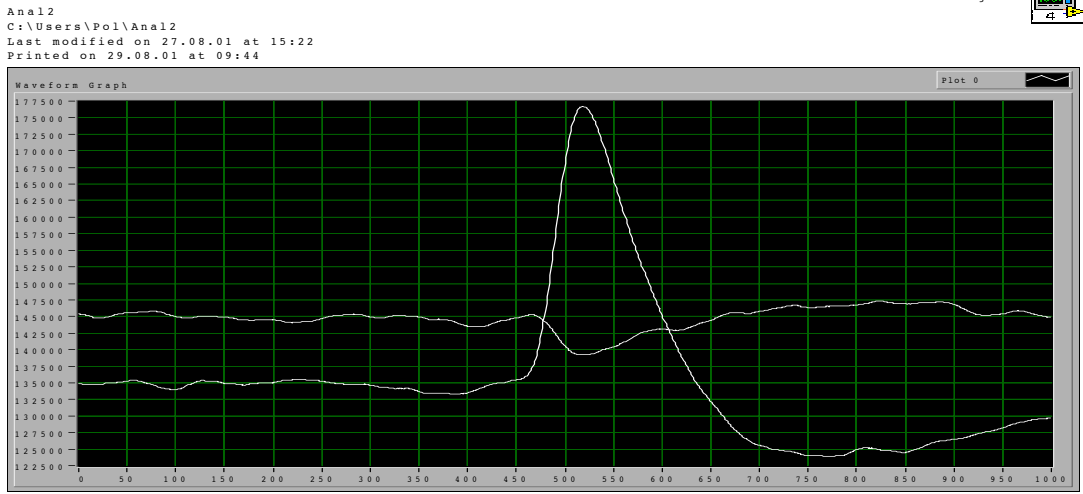


Figure 6.2: Superposition of 1000 events with a high voltage of  $-1.5\text{kV}$  and  $+2.5\text{kV}$ . The horizontal scale is 25 ns per division and the vertical scale 25V per div. (for all the next Figures is the same scale)

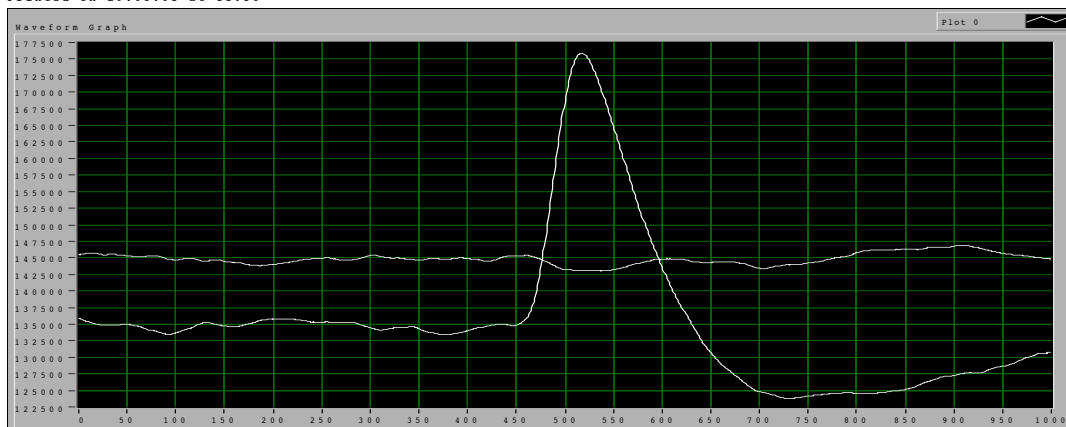


Figure 6.3: Superposition of 1000 events with a high voltage of  $-1.5\text{kV}$  and  $0\text{V}$

### Cathode high voltage $-2.5\text{kV}$

When the cathode high voltage is set to  $-2.5\text{kV}$  a positive anode signal appears (see Figs.6.4 and 6.5), this could be probably due to electrical breakdowns of the connectors; in fact, once the set-up was opened the LAr level was below them.

Anal2  
 C:\Users\Pol\Anal2  
 Last modified on 27.08.01 at 15:22  
 Printed on 29.08.01 at 10:09

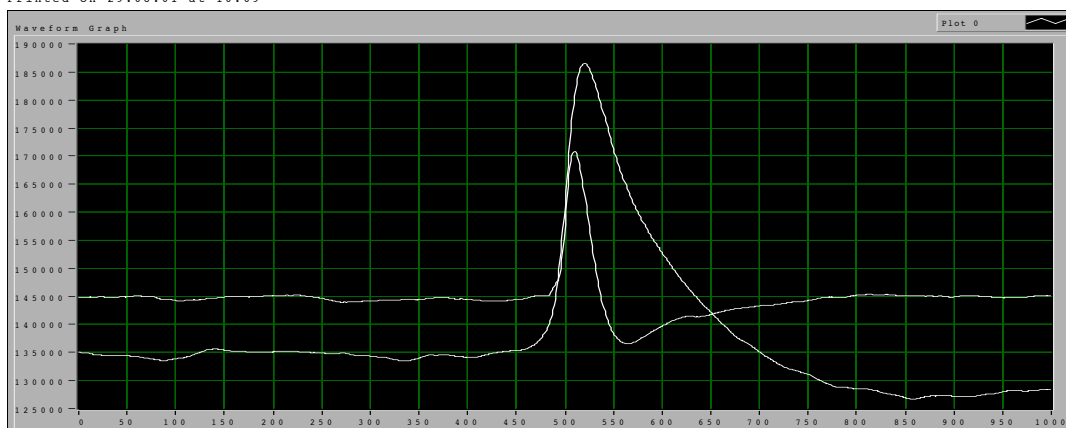


Figure 6.4: Superposition of 1000 events with a high voltage of  $-2.5\text{kV}$  and  $+2.5\text{kV}$

Anal2  
 C:\Users\Pol\Anal2  
 Last modified on 27.08.01 at 15:22  
 Printed on 29.08.01 at 10:05

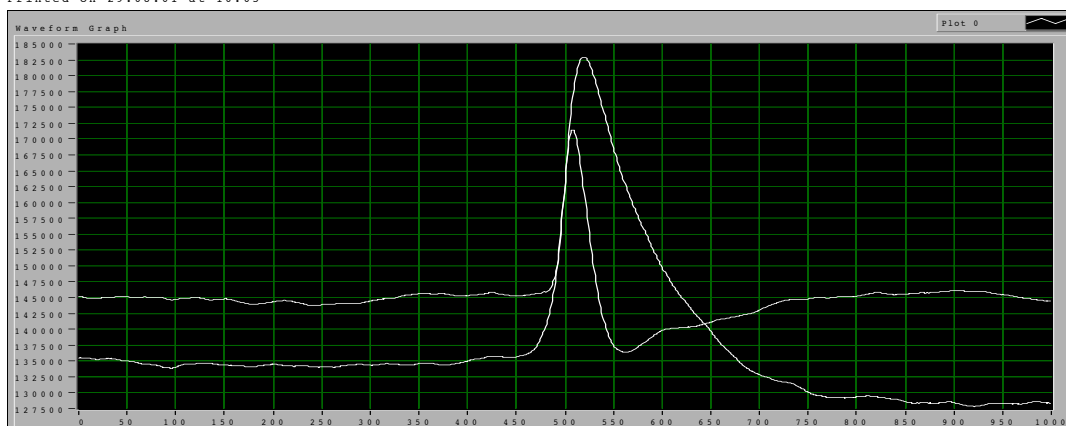


Figure 6.5: Superposition of 1000 events with a high voltage of  $-2.5\text{kV}$  and  $0\text{V}$

## 6.2.2 Trigger on the anode

The trigger was set to the anode signal with a threshold of 1010 channels on the PC card. The two measurements are shown in Figs. 6.6 and 6.7, they differ in the high voltage applied to the electrodes. In both cases no cathode signals are present. A possible explanation is that the  $\gamma$ 's emitted from the source with a probability of 9.4% and an energy of 1.27 MeV (see 2.1.3) create an ionizing electron with photoeffect or Compton scattering. In the first case the  $\gamma$  hitting the stainless steel disc of the anode creates an electron which is energetic enough to escape from the anode and consequently ionizes the LAr giving a signal of an incoming electron cloud. The second possibility is that an electron is produced when it scatters with the photon, this will give a signal if such an event is close enough to the anode so that the electrons created by ionization will induce a detectable signal. The height of the induced signal depends on the charge acceleration and consequently on the electric field strength, which decreases with the distance. This is demonstrate in the Figs. 6.6 and 6.7, because the mean signal height is bigger for the larger voltage.

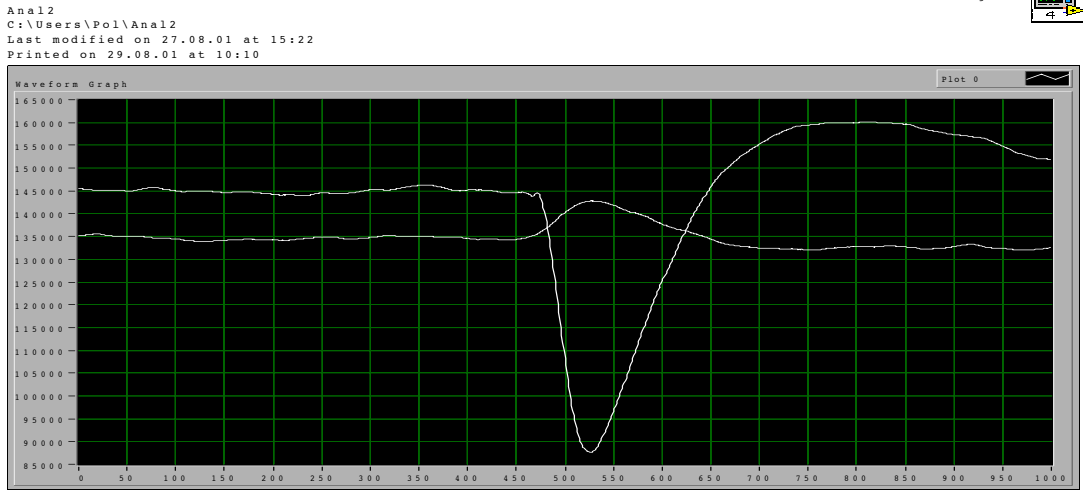


Figure 6.6: Superposition of 1000 events with a high voltage of  $-2.5\text{kV}$  and  $+2.5\text{kV}$

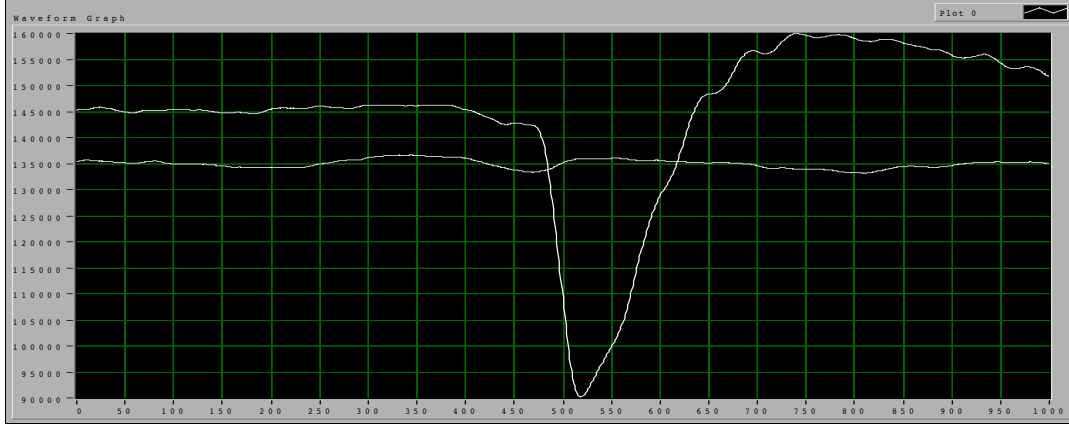


Figure 6.7: Superposition of 1000 events with a high voltage of  $-1.5\text{kV}$  and  $1.5\text{kV}$

### 6.3 Discussion of the measured charge distribution

To obtain the number of electrons corresponding to a measured pulse, the first step of the data acquisition of section 6.1 has been performed. The signals measured are compared with those of the calibration, thus, the corrected signal height and consequently the number of electrons can be found. The histogram obtained from the comparable measurements 1 and 2 (the HV at the cathode is the same, see Tab.6.2) is shown on Fig.6.8. This histogram is not compatible with the (calculated) spectrum from the decay positrons with end point energy of  $1.83\text{MeV}$  (taking into account the energy loss of about  $0.4\text{MeV}$  of the positrons in the silver foil (see Fig.6.9)).

There are two reasons for this discrepancy:

1. the silver foil is not thick enough to stop all the positrons from the decay mode with end point energy of  $0.543\text{MeV}$ ;
2. as mentioned in section 6.2.2 the  $\gamma$ 's can produce an electron by Comp-

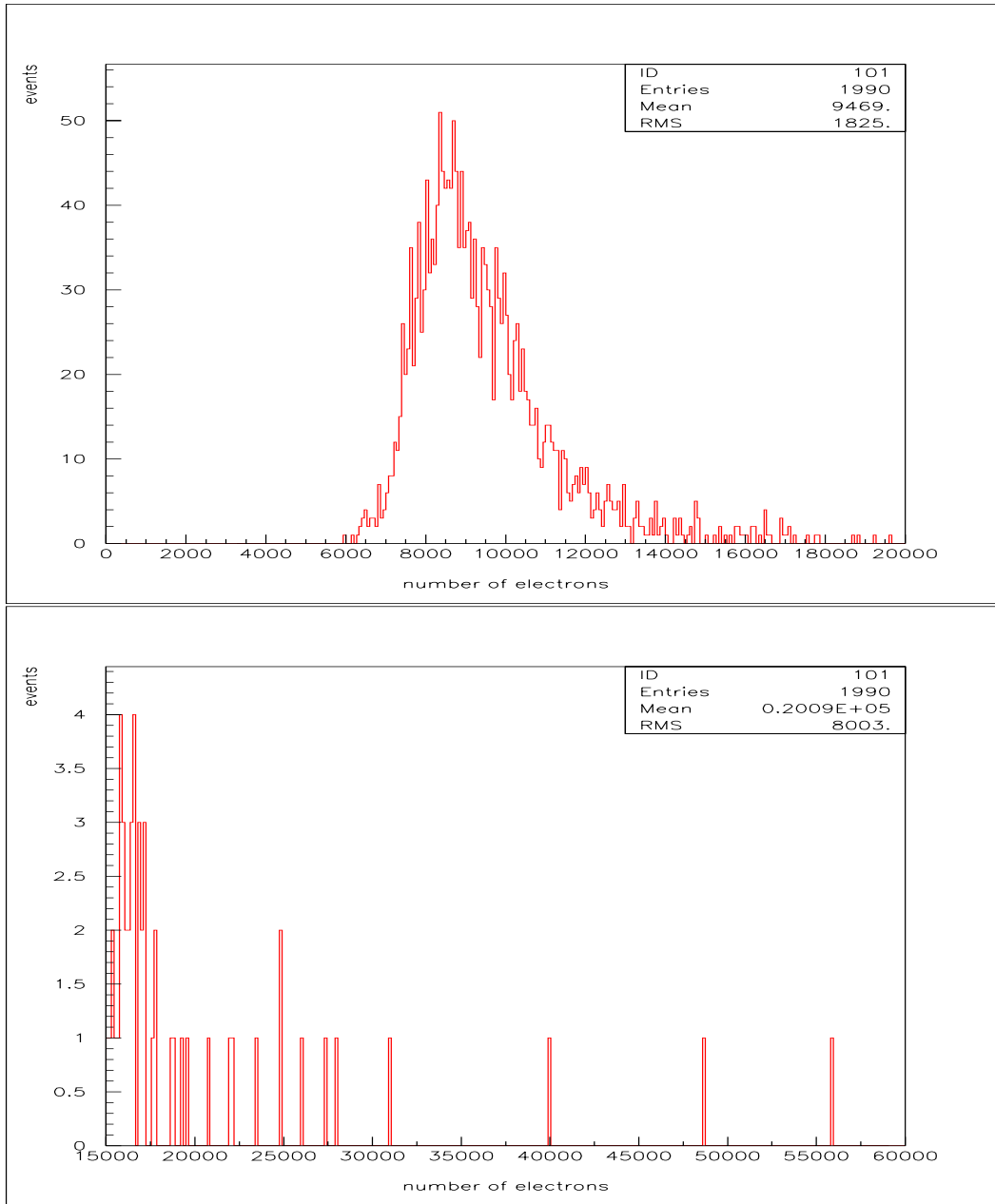


Figure 6.8: Histogram of the number of measured electrons.

ton scattering; this electron ionizes the LAr and induces a signal on the cathode.

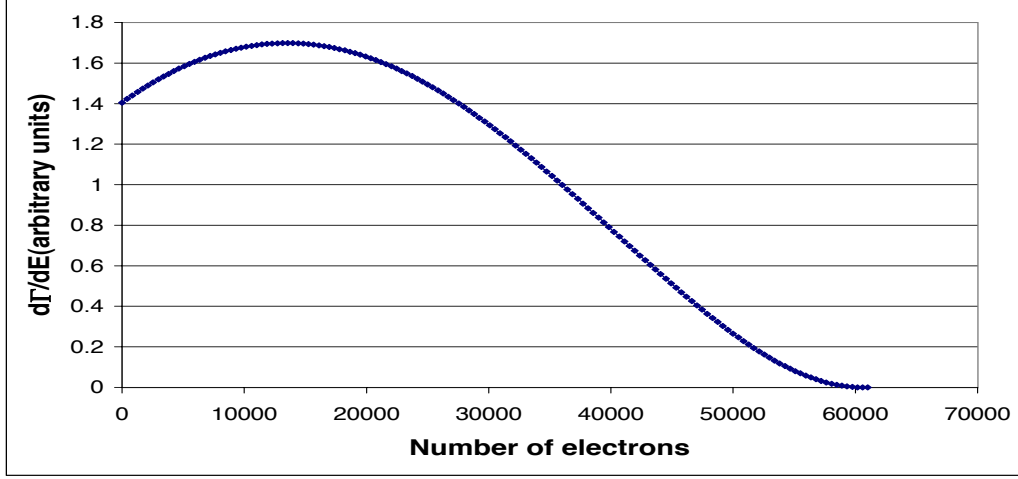


Figure 6.9: Spectrum of the positrons emitted from the cathode taking into account the energy loss in the silver foil

The first reason can be demonstrated measuring the activity of the source with and without the silver cover and then calculating the expected number of electron created. To estimate the contribution of Compton scattering to the event rate, the number of electrons created by a Compton electrons as first to be calculated. The energy spectrum of the Compton electrons is sketched in Fig.6.10 [14]. The parameter  $\epsilon$  is the ratio of the photon energy (1.27MeV) and the electron mass (0.511MeV):

$$\epsilon = \frac{h\nu}{m_e} = 2.48 \quad (6.1)$$

The maximal energy transfer takes place when the electron is forward scattered and the photon backward and can be calculated with:

$$T_{max} = \frac{h\nu}{1 + 1/2\epsilon} = 1.05MeV \quad (6.2)$$

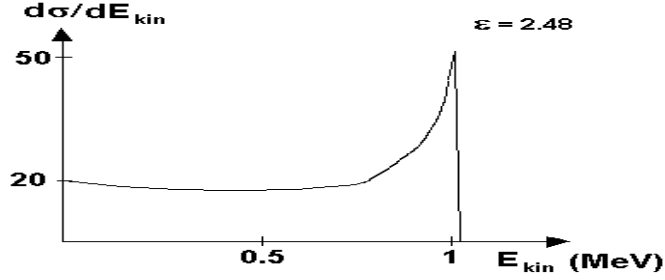


Figure 6.10: Energy spectrum of the Compton electrons

The ratio  $R$  between the expected number of events from a ionizing particle (a positron or a Compton electron) with initial kinetic energy smaller than 1.05MeV and the number of events produced by a positron with energy bigger than this treshhold is given by:

$$R_{estimated} = (\Gamma_{Compton} + \Gamma_{e^+(1.83MeV)}^- + \Gamma_{e^+(0.543MeV)}) / \Gamma_{e^+(1.83MeV)}^+ \quad (6.3)$$

where  $\Gamma_{Compton}$  is the relative rate of the electrons produced by Compton scattering,  
 $\Gamma_{e^+}^\pm$  is the relative rate of the positrons with energy smaller (-) or bigger (+) than 1.05MeV from the decay mode with end point 1.83MeV,  
 $\Gamma_{e^+(0.543MeV)}$  is the relative rate of the positron with spectrum end point 0.543MeV that pass through the silver foil and have enough energy ( $E > E_{th}$ ) to give a signal above the trigger threshold.

From the Fig.6.8 one can extract the trigger threshold, which is about 6000 electrons. This is equal to the number of electrons generated by a particle with 0.14MeV energy, hence,  $E_{th}=0.14\text{MeV}$ .

To estimate  $\Gamma_{Compton}$  one has to make the assumption on the maximal distance  $x_{max}$  from the cathode at which a Compton electron with energy bigger than  $E_{th}$  will produce a signal larger than the trigger treshhold. Once this value is fixed  $\Gamma_{Compton}$  is given as follows:

$$\Gamma_{Compton} = 9.4 \cdot 10^{-2} (1 - e^{-x_{max}/\lambda}) \cdot W_c(E_{th}) \quad (6.4)$$

where  $\lambda$  is the attenuation lenght of photons in LAr and is approximately 15 cm ([13] at page 152).  $W_c(E_{th})$  is the probability that the Compton electron has an energy between  $E_{th}$  and  $T_{max}$ . With  $E_{th}=0.14\text{MeV}$  it follows from Fig.6.10 that  $W(E_{th})=87\%$ . Assuming  $x_{max}=0.3\text{cm}$  and substituting these values in Eq.6.4 gives  $\Gamma_{Compton} = 1.6 \cdot 10^{-3}$ .

The relative rate of the positrons from the decay mode with end point energy of 1.83MeV and a probability of emission of 0.06% is given by:

$$\Gamma_{e^+(1.83)}^\pm = 0.06 \cdot 10^{-2} \cdot W^\pm(E_{th}) \quad (6.5)$$

where  $W(E)^\pm$  is the probability of the positron to be emitted with energy smaller (-) or bigger (+) than  $E_{th}$ . With the values  $W(E_{th})^+=8\%$  and  $W(E_{th})^-=92\%$  extracted from Fig.6.9, one obtains  $\Gamma_{e^+}^- = 4 \cdot 10^{-4}$  and  $\Gamma_{e^+}^+ = 5 \cdot 10^{-5}$ .

The relative rate of the positrons coming from the spectrum with end point energy of 0.543MeV is:

$$\Gamma_{e^+(0.543)} = 90.6 \cdot 10^{-2} \cdot W_{0.543}(E_{th}) \quad (6.6)$$

$W_{0.543}(E_{th})$  is the probability that a positron has an energy bigger than the energy treshhold  $E_{th}=0.14 \text{ MeV}$ . To estimate  $W_{0.543}(E_{th})$ , we use the ratio of rates measured with a beta-counter for the source covered by silver foils and the uncovered source; this ratio is 1/5. Using Fig.2.4 the maximal energy that a positron has after it passes through the silver foil is 0.23MeV and consequently  $\Gamma_{e^+(0.543)} = 1.7 \cdot 10^{-2}$ . To note is that a positron with energy in the order of 0.23MeV will give a signal that is equivalent to about 9700 electrons, which corresponds roughly to the peak of the measured events (see Fig.6.8).

Substituting the values calculated for the relative rates in Eq.6.3 one obtains:

$$R_{estimated} = 350.$$

From the data:

$R_{measured} = (\text{Total number of events}) / (\text{events} > 45000 \text{ electrons}) = 1990 / 2 = 432$ ,  
 where 45000 electrons is the value that an electron of 1.05MeV will produce  
 if it starts from the surface of the cathode.

The ratio between  $R_{estimated}$  and  $R_{measured}$  is:

$$R = R_{estimated} / R_{measured} = 81\%,$$

thus, we conclude that what we observe is what we expected within the  
 uncertainty of our estimates and statistical measurements.

# Chapter 7

## Conclusions

The signals from the cathode and from the anode have been seen, but no events with both pulses, the cathode and the delayed anode signal, were observed. This is probably due to the fact that the LAr was not pure enough and the starting electrons were captured during the drift by the impurities. Most of the signals from the cathode are produced by the positrons with end point energy 0.543MeV emitted by the  $^{22}\text{Na}$  source with a decay ratio of 90.6%. These were initially meant to be eliminated by the silver foil that covers the source, but from the measurements one can conclude that about 1.7% of these positrons give a signal above the trigger threshold. To demonstrate is that using a thicker silver foil the positron of the end point spectrum 0.543 MeV are stopped.

Two events with a charge bigger than 45000 electrons(corresponding to a deposited energy of 1.05MeV) were observed. The signals of the positrons with spectrum with end point energy of 1.83MeV and energy bigger than 1.05MeV should be easily discriminable from those of the electrons produced by Compton scattering. In fact the relative rate of the Compton, integrated over the whole measured spectrum, is 3 times larger than that of the positron from decay mode with the end point 1.83MeV, hence, there is no problem with pile-up.

# Acknowledgements

I would like to thank Prof. Dr. André Rubbia for giving me the possibility to make the diploma work in his group and learning very much and for his advice. Thanks also to Dr. Andreas Badertscher and PhD Student Marco Laffranchi for their suggestions and their disponibility, to Mr. Scherrer and Mr. Filsner for their help and last but not least to Rosa, Gusti, Leo, Markus (computer consulting), Marc (official cigarettes sponsor) and pcicarus4.

# Bibliography

- [1] *The ICARUS Experiment, Initial Physics Program*. LNGS-P28 (2001)
- [2] *Stopping Power for Electrons and Positrons*. ICRU Report No.37 (1984)
- [3] J.F.Ziegler. *The Stopping and Range of Ions in Solids*. Pergamon Press, Inc.(1985)
- [4] M.Laffranchi. *Development of a new LAr Purity Monitor: Design of the  $\alpha$ -Source*. Diploma thesis, ETH Zürich (2000)
- [5] R.Vandenbosch and J.R.Huizenga.*Nuclear Fission*. Accademic Press (1973)
- [6] F.Hölldorfer and W.Walkowiak. *A Study of the Sensivity of the Purity Monitor for th e ATLAS LAr Calorimeters*. ATLAS International Note LARG-NO-089 (1998)
- [7] *ICANOE proposal*. CERN/SPSC 99-25 (1999)
- [8] J.Thomas and D.A.Imel. *Recombination of electron-ion pairs in liquid argon and liquid xenon*. Phys.Rew.A 36,614 (1987)
- [9] F.Halzen and A.D.Martin. *Quarks & Leptons*. John Wiley & Sons, Inc.(1984)
- [10] E.A.Uehling. *Penetration of heavy charged particle in matter*. Annual Rev. Nucl.Sci.4,315 (1954)
- [11] A.M.Kailinin et al. ATLAS International Note, ATLAS-LARG-NO-058, CERN (1996)

- [12] M.Brimmeyer. *Data acquisition of a new LAr Purity Monitor: Designed with an  $\alpha$ -Source*. Diploma thesis, ETH Zürich (2001)
- [13] Caso et al. *Particle Data Book* Review of Particle Physics (1998)
- [14] P.Marmier *Kernphysik I* VMP-Verlag ETH Zürich (1965)